MULTI-SCALE MODELLING OF OXIDE-BASED SOLID STATE BATTERY.

By

Refiloe Innocencia Maphoto

RESEARCH DISSERTATION

Submitted in fulfilment of the requirements for the degree of

Master of Science (MSc)

In

Physics

In the

Faculty of Science and Agriculture,

(School of Physical and Mineral Sciences)

At the

UNIVERSITY OF LIMPOPO

SUPERVISOR: Prof R. S. Ledwaba

Co-SUPERVISOR: Dr M. C. Masedi

: Prof P. E. Ngoepe

2022

Declaration

I declare that the dissertation hereby submitted to the University of Limpopo, for the degree of asters of science in Physics has not previously been submitted for a degree at this or any other university; that it is my work in design and execution, and that all material contained herein has been duly acknowledged.

29/08/2022

Maphoto R.I.

Date

Abstract

The oxide garnet $Li_7La_3Zr_2O_{12}$ (LLZO) exhibits high Li-ion conductivity and chemical stability when in contact with lithium metal anodes, making it a promising solid electrolyte for Li-based batteries. The tetragonal phase, however, is poorly Li-ion conductive at room temperature. It is essential for Tetragonal $Li_7La_3Zr_2O_{12}$ (t-LLZO) to be capable of enduring high temperatures with good phase stability in order to be used in practical devices. In this way, adding supervalent cations, such as Ta, to the Zr-site of t-LLZO stabilizes the low-temperature structure of the tetragonal crystals, and more importantly, creates vacancies in the tetragonal phase, thereby enhancing its ionic conductivity. However, the crystal structure behaviour at high temperatures remains unclear. Moreover, the fundamental aspect of supervalent substitution as well as which level of lattice expansion/contraction promotes ionic diffusion of this supervalent substitution remains poorly understood.

The density functional theory calculations implemented in the Vienna ab initio simulation package were utilized to offer a better understanding of the stabilization of the tetragonal $Li_7La_3Zr_2O_{12}$ phase by determining the structural, mechanical, and electronic properties of the high-conductive LLZO structure. It was found that the structural properties calculated are in good agreement which is within a 2% error of the experimentally measured results from other studies. The t-LLZO structure has a negative energy of formation, which is consistent with experimental data. The calculated Young's modulus is in good agreement with the experimental observations, and it satisfies the necessary stability constraints for the configuration. Owing to its large band gap for electrochemical stability, the calculated band structure of t-LLZO shows that the material is a magnetic separator with a wide and indirect band gap along the g-symmetry point, which is in good agreement with the experimental observations from other studies.

In this study, first-principle calculations combined with cluster expansion simulation were performed on the t-LLZO to attain a fundamental understanding on the phase stability of Ta-doped LLZO and generate new possible phases of Ta-doped LLZO. Furthermore, Monte Carlo simulation was utilised to gain an insight into the behaviour of the Ta-doped phase as a function of temperature under canonical ensemble. The cluster expansion generated 28 new multi-component Ta-doped $Li_5La_3Zr_{2-x}Ta_xO_{12}$ structures, were all of the new structures are thermodynamically stable with a negative enthalpy of formation. The Monte-Carlo temperature profiles have a miscible gap with very small energy difference, indicating that there is no phase separation and the system mixes well at ~900K. Further density functional theory calculations were performed on the most stable generated Ta-doped LLZO structures to determine the structural, mechanical, and electronic properties of the structures for their application as active solid-state electrolytes. It is found that the generated structures exhibit good structural stability since the calculated lattice parameters of the Ta-doped LLZO structures are found to be smaller than that of pure t-LLZO. The results show that the distance between Li-Li in doped Ta-LLZO is smaller than in pure t-LLZO, which indicates that the smaller the difference between the dopant ionic radius and the critical dopant radius, the higher the conductivity. Therefore, the structural properties of Tantalum-doped structures are shown to improve due to the smooth decrease in calculated lattice parameters. Moreover, the Ta-doped structures show good elastic stability against deformation and exhibit magnetic separator behavior, which encourages their use as the next-generation solid electrolytes. Therefore, the findings provide a better understanding of the phase stability of the generated Ta-doped LLZO structures, which set a strong foundation for further analysis of the temperature effect on the rate of lithium-ion diffusion and the mobility of the lanthanum, zirconium, tantalum, and oxygen ions in the system at high temperatures, which is crucial for the development of these promising solid-state electrolytes for all-solid-state Li-ion batteries.

Acknowledgements

I would like to take this opportunity to thank my supervisor: Prof R.S. Ledwaba and co-supervisors: Dr. M.C. Masedi, and Prof P.E. Ngoepe for their support, patience, encouragement, and discussions during the project.

My sincere appreciation to Dr. K.T. Malatji for the great discussions during the cluster expansion simulations, I am always enlightened after our discussions.

This work was performed using the computational facilities of the Centre for High Performance Computing (CHPC), Cape Town and Materials Modelling Centre at University of Limpopo, in South Africa. The financial support from the National Research Foundation (NRF) Thuthuka (Grant Unique Number: 121850) is acknowledged.

Dedication

This work is dedicated to my grandmother, *Maria Ledile Shokane*. Your prayers, love, and guidance have led me to where I am today. Continue to rest in peace.

Kea leboga Mosengwana.

Table of Contents

List of figures

List of tables

CHAPTER 1: Introduction

In this chapter, a brief literature review of the oxide-garnet $Li_7La_3Zr_2O_{12}$ (LLZO) solid-state electrolyte and their functionality in batteries are presented. First, a basic background of batteries is presented to give a clear view of what batteries are, followed by the history of batteries, which gives details on how batteries came about or rather the invention of batteries. With the interest study based on the solid-electrolyte as a function of Li-ion batteries, a detailed general introduction on the all-solid-state Li-ion batteries is given, as well as the advantages and disadvantages of All-solid-state lithium ion batteries (ASSLIB). The applications of ASSLIB are detailed to give an insight into why it is crucial to improve solid-state LLZO for better development of ASSLIB. A brief discussion on solid-state electrolytes as the main topic of the study is to clarify the importance behind them. Challenges concerning the electrolytes are also reviewed in this section. Doping as an approach believed to help improve the electrolyte and generate stable structures is discussed. The crystal structure of oxide-garnet LLZO solid-state electrolyte is reviewed, and lastly, the rational, as well as the aims and objectives of this study are reviewed.

1.1 General introduction

Improving battery technology is a critical need for modern technology and a major goal for many researchers. Since the discovery of electricity, effective methods to store energy for usage are on demand. Over the last century, the energy storage industry has continued to evolve, adapt, and innovate in response to changing energy requirements and advances in technology. Energy storage systems provide a wide array of technological approaches to managing power supply to create a more resilient energy infrastructure and bring cost savings. Batteries are a range of electrochemical storage solutions, including advanced chemistry batteries, flow batteries, and capacitors [1].

Batteries serve a variety of functions in daily life, ranging from delivering the initial power required to start automobile engines to serving as a backup source of electricity in telecommunications, public transportation, and medical applications. The batteries also minimize greenhouse gas emissions by storing electricity generated from both traditional and renewable sources. Figure 1.1 shows the anode, cathode, separator, and electrolyte components of a lithium-ion battery [2]. To achieve energy storage, lithium-ions are released from the positive electrode. The electrolyte carries positively charged lithium ions from the anode to the cathode and vice versa through the separator. The movement of the lithium ions creates free electrons in the anode creating a charge at the positive current collector. The electrical current then flows from the current collector through a powered device (the bulb) to the negative current collector. The separator blocks the flow of electrons inside the battery. The battery takes in and stores energy during this process.

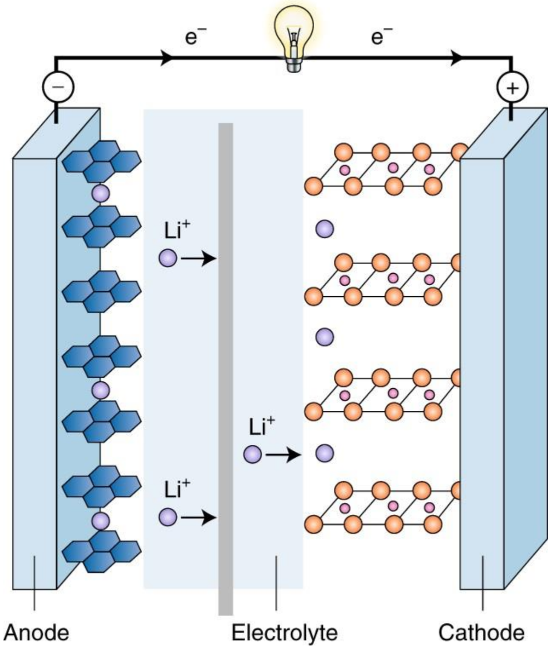

Figure 1.1: Diagram of the basic components of a lithium ion battery *[2]*.

1.1.1 Brief description of all solid-state lithium ion batteries

The need for lithium-ion battery systems with high energy density and exceptional safety has increased in lockstep with the rapid development of new energy technologies. Because liquid electrolytes have extremely high ionic conductivities, in the region of 10^{-3} S/cm, they are used in the bulk of Lithium ion batteries (LIB). However, major issues such as flammability, leakage, and the growth of dendrites in the electrodes plague these liquid electrolytes, driving demand for safer lithium-ion batteries [3]. To this end, the concept of all-solid-state lithium ion batteries based on solid electrolytes has been proposed and has been gaining traction due to its inherent safety, high energy density, and potentially long life cycle in that it may improve battery configuration efficiency, as well as the use of metallic Li anode and high-voltage cathode [4].

The packaging of a battery can also be simplified when it is made entirely of solid-state materials, as shown in Figure 1.2. As a result, for the same type of active material, less packaging is required, and ASSLIBs are expected to have a lower self-discharge and higher volumetric energy density than conventional batteries [5] . Various solid-state electrolytes with multiple phases, among the existing SSEs, provide more flexibility in customizing and combining the advantages of single-phase electrolytes, which have been actively explored recently and are regarded as attractive commercial options. Solid state electrolytes (SSE) with appropriate ion concentrations are needed for the future development of ASSLIBs.

A battery technology that uses solid-state technology has the following advantages: faster charging. In 15 minutes, solid-state batteries can charge 80 percent, suggesting they will perform at least as well as lithium-ion batteries. The energy density is higher, indicating that it might have a range of two times or even more than the current range. It also has a higher voltage and a longer life cycle. Solid-state batteries, however, carry a risk or two, including dendrites, which are root-like growths that can form inside a solid-state battery, causing the battery to fail by interfering with the precise separation of material layers. Solid-state batteries are easily affected by the natural changes that occur during charging and discharging. These movements might degrade the tight, exact arrangement of solid-state components, possibly leading to the failure of the battery.

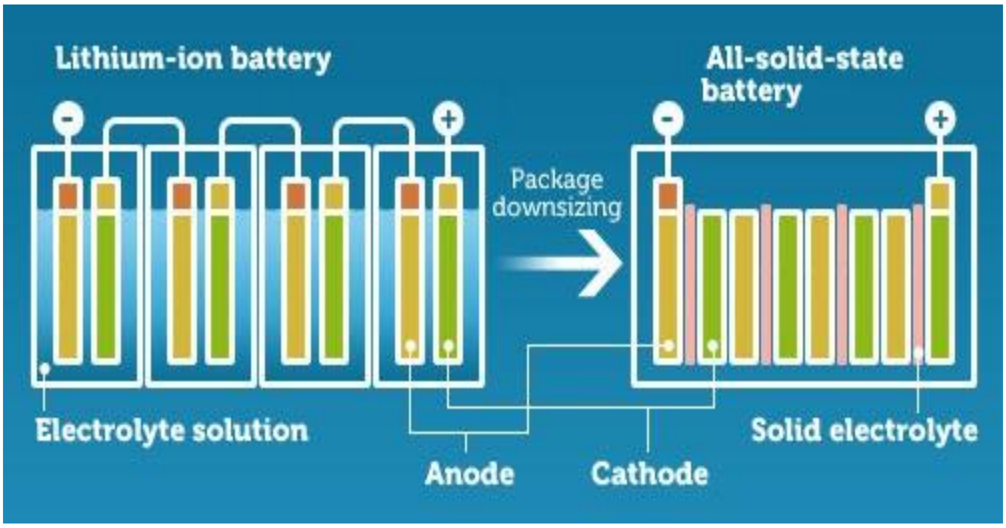

Figure 1.2: Illustration of the packaging size of lithium ion battery when the liquid electrolyte is replace by solid electrolyte *[5]*.

1.1.2 Applications of all solid-state lithium ion batteries

Solid-state lithium ion batteries are a promising energy source for the future generation of electronic devices, paving the way for mobile electronics in the coming ubiquitous computing society as well as pollution-free pure electric automobiles. As previously said, solid state Li-ion batteries come in a variety of shapes and sizes. Furthermore, regardless of the system's size, this makes them the ideal choice for power demands. ASSLIB also offers a wide range of power solutions, from energy storage to portable energy. Power backups/UPS, electric mobility, energy storage systems mobile, laptops, and other regularly used consumer electronic items are among of the most prevalent applications of solid-state lithium-ion batteries. When compared to ordinary lithium ion batteries, solid-state Li-ion batteries are increasingly used for a variety of applications. The fundamental driving force for the development of solid-state batteries in numerous industries is safety [6].

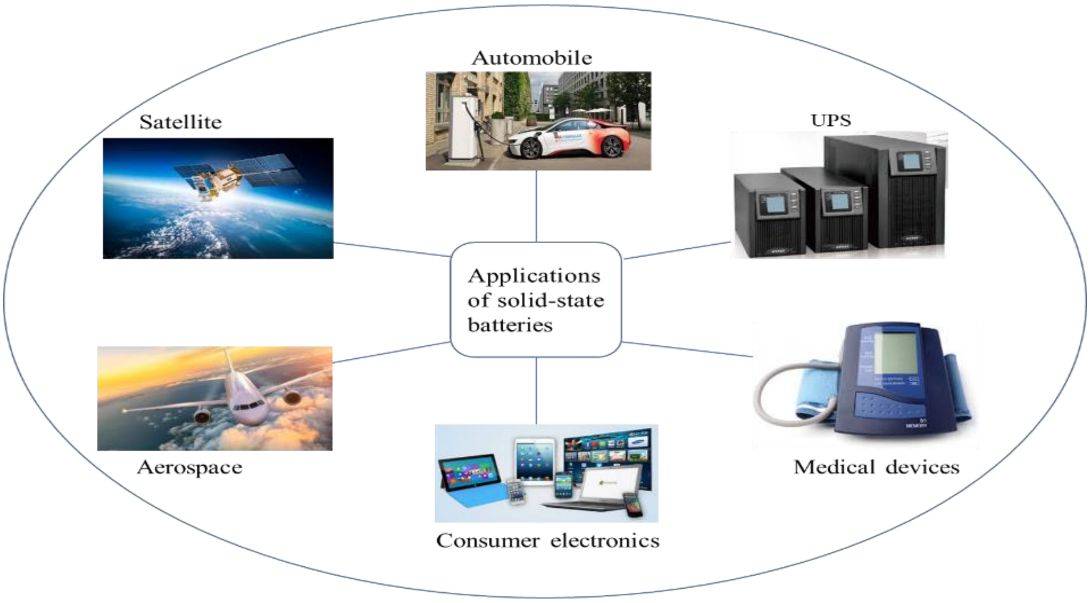

Figure 1.3: Applications of solid-state lithium-ion batteries.

1.2 Literature review

1.2.1 Solid state electrolytes

Solid-state electrolytes (SSE) have recently received a lot of attention for its potential use in next-generation all-solid-state lithium-ion batteries. Solid electrolytes conduct lithium ions at ambient temperature and could eventually replace flammable and toxic organic electrolytes. Solid-state electrolytes allow the use of lithium metal as the anode, in addition to greatly enhancing the battery's safety. As a result, the cell voltage rises, increasing the battery's energy density.

The development of highly ionic conductive solid materials for many purposes, particularly for rechargeable lithium ion batteries, has sparked a lot of study. In order to construct a high Li+ ion conductive solid electrolyte, many inorganic materials such as sulfide, oxide, iodide, chloride, and others have been studied [7]. Solid electrolytes of sulfide, oxide, phosphate, and silicate have all been used in ASSBs [8]. All electrolytes, however, have some drawbacks. Their low ionic conductivity is the first. The second is solid electrolyte electrochemical and chemical stability. Because the solid electrolyte in ASSBs comes into touch with highly oxidized cathode material and strongly reduced anode material, the electrochemical window is a critical characteristic. Some solid electrolytes, such as those containing Ti ions, can be lowered using Li-doped graphite or Li metal [9].

Due to the fact that sulfur can react with oxygen to form SOx, ASSB with sulfide solid electrolyte may ignite in the event of an accident. The combustion of an all-sold state battery, on the other hand, is substantially slower than a normal lithium ion battery with organic electrolyte. Oxide solid electrolyte is safer than organic liquid and sulfide solid electrolyte in ASSBs. Hence, the oxide type with garnet-like structural inorganic solid Li ion conductive $Li_7La_3Zr_2O_{12}$ (LLZO) received considerable attention in recent times due to its superior conductivity (~10^{-4} $S.cm^{-1}$) at room temperature, safety and excellent stability with metallic lithium [10, 11].

The highest lithium-ion conductivity is found with the cubic phase (space group $Ia\overline{3}d$) of $Li_7La_3Zr_2O_{12}$ garnet [12].“However, at room temperature, a low-energy ordering of Li into the 16f, 32g (octahedral) and 8a (tetrahedral) sites of the tetragonal structure, can occur, reducing symmetry to $I4_1/acd$ (tetragonal phase) [13]. The conductivity of the tetragonal phase at room temperature is ~2 orders of magnitude lower than that of the cubic phase [14, 15]. Thus, the challenge has been to stabilize both cubic and tetragonal phases of LLZO. However, the phases can be stabilized by creating Li vacancies through supervalent cation doping such as Al^{3+}, Ga^{3+}, on the Li-site or Ta^{5+}, Nb^{5+} on the Zr-site.

The Al^{3+} ions were the first to investigate the stabilization of the LLZO structure with cubic geometry in 2011. Al has been shown in several experiments to help stabilize the cubic phase at ambient temperature while also increasing ionic conductivity [16]. According to Bonilla et al., Al substitution in tetrahedral sites of the tetragonal LLZO opens previously inaccessible sites, improving Li-ion conductivity [17].

Due to the variety of multicomponent solid electrolytes, the first-principle cluster expansion calculations provide a powerful tool for efficiently searching for new stable structures. It is therefore essential to consider LLZO phase stability and to identify the most effective dopant for increasing LLZO ionic conductivity.

1.2.2 Advantages of solid electrolytes

Solid electrolytes play a crucial role in all-solid-state LIBs. Utilizing solid electrolytes to improved battery performance can result in the following benefits: Oxide-based inorganic materials retain their stability at high temperatures. The conductivity of some solid electrolytes is higher than that of liquid electrolytes [18]. In LIBs, high-voltage Li cathode materials can be used due to the chemical stability of solid-state electrolytes over liquid electrolytes. In contrast to metallic Li, high electrochemical stability windows up to 6 V have been found [19, 20]. As solid electrolytes have a great deal of mechanical strength, dendrite development can be greatly reduced, thus allowing the use of high-energy dense metallic lithium as an anode in all-solid-state batteries.

Another benefit of solid-state batteries is their long lifespan. In a liquid electrolyte, all species other than Li^+ ions move, including counter-anions, solvent molecules, and contaminants. When a species migrates to the surface of the cathode, it may be oxidatively destroyed, or it may be reduced when it reaches the surface of the anode. That is, migration may produce side reactions in the batteries, resulting in a reduction in battery performance. In solid electrolytes, however, only lithium ions diffuse. It means that such species do not move about, causing side effects to occur. As a result, solid-state batteries have a long cycle life, a long shelf life, and a low self-discharge rate [21, 22]. Finally, the electronegativity of oxide ions is high. It indicates that electrons in oxide electrolytes are rarely lost, and they are resistant to electrochemical oxidation. As a result, oxide electrolytes will work with high-voltage electrodes.

1.2.3 Doping

Doping is a common method of altering material properties in which one or more elements or compounds are doped into the substrate to produce or improve specified attributes. Due to its high energy density and chemical stability with respect to Li metal anode, the oxide garnet $Li_7La_3Zr_2O_{12}$ (LLZO) is a viable solid electrolyte for Li-ion batteries. However, it crystallizes into a poor Li-ion conductive tetragonal phase at low temperature. The most effective technique to stabilize the tetragonal phase lattice and improve ionic conductivity is through element doping. On the one hand, element doping can effectively increase the lithium vacancy concentration and the disorder of the lithium-ion arrangement in the lattice, hence stabilizing the tetragonal phase and maximizing the ionic conductivity. In addition, the skeleton structure of LLZO lattice can be adjusted by element doping to increase the lithium ion mobility.

Li site, La site, and Zr site are the three different types of doping and substitution sites for LLZO. Doping at different places has distinct effects on LLZO ionic conductivity. To partially substitute the Li element when doping at the Li site, researchers commonly utilize Al^{3+}, Ga^{3+}, Fe^{3+}, and other elements. The substitution of the Li site only influences the concentration of lithium ions in LLZO, and research has shown that the concentration and distribution of lithium ions in LLZO have a significant impact on its ionic conductivity. Rangasamy et al. [23] discovered that doping LLZO with 0.2-0.24 mol Al stabilizes the cubic phase, and their ionic conductivities are higher than LLZO without Al doping. This phenomenon was quickly confirmed by other researchers who also studied Al-doped LLZO [24, 25].

The La site element doping has a greater influence on the entire crystal structure of LLZO and determines the bottleneck size of the lithium ion transport [21]. Therefore, it is difficult to find suitable doping ions for the La site. The supervalent doping of the Li and La sites causes lithium vacancies and disordered lithium sub-lattices. In contrast to supervalent doping, low-valence doping results in excess lithium ions. It was reported that doping at the La site with a relatively large-radius cation could enhance the conductivity of LLZO. Jiang-Fang Wu et al. [26] doped cation Rb^+ at the La^{3+} site in cubic $Li_{6.10}Ga_{0.30}La_3Zr_2O_{12}$, which led to a highest ionic conductivity of 1.62 mS/cm at 25°C.

Doping cations on both La and Zr sites is believed to generate synergistic effect on LLZO for fast Li^+ conduction [27]. Very recently, Ca was also reported to enhance the ionic conductivity by incorporating with Ta, indicating a promising approach to higher ionic conductivity [28]. Several studies revealed that Al can help stabilization of cubic phase at room temperature and increases the ionic conductivity [29, 30].

For this study the focus is on the Zr site of the t-LLZO since it has the Wyckoff equation of (0, 0, 0), also because the Li site is fully ordered. Moreover, Ta doping on the Zr site of the tetragonal LLZO allows previously inaccessible sites to become available, which enhances Li-ion conductivity. The supervalent cation Ta^{5+} is partially doped at the 16c of Zr^{4+} site to improve the stability of t-LLZO and to generate new possible stable Ta-doped LLZO phases with high ionic conductivity. Each doping concentration plays a significant role in changing the garnet framework in strategic doping in the t-LLZO garnet. As a result, identifying the appropriate doping concentration can significantly improve Li-ion conductivity in t-LLZO.

1.3 Structures of Garnet-type oxide solid electrolyte

The garnet-type material tetragonal $Li_7La_3Zr_2O_{12}$ known as t-LLZO with the space group $I4_1/acd$ which has the highest ionic conductivity has been introduced by Murugan et al. in 2007 [13]. The generic formula for LLZO garnet $Li_7La_3Zr_2O_{12}$ has been derived from the garnet type family $Li_7A_3B_2O_{12}$ in which Li ions can occupy octahedral and tetrahedral sites, A-cations belong to eight-coordination sites and B-cations belong to six-fold coordination sites. Table 1.1 shows the t-LLZO unit cells lattice parameters: a=b=13.12Å, c=12.67Å, angle: $\alpha = \beta = \gamma =$

90◦, with space group $I4_1/acd$. The crystal structure of t-LLZO as shown in Figure 1.4 consists of individually fully occupied lithium sites (colored yellow) within the crystal lattice: Li(1) is located at the tetrahedral 8a site connected to six O atoms, whereas Li(2) and Li(3) are located at the octahedral 16f and 32g sites, respectively, and both are connected to four O atoms. Dodecahedral La(1) and La(2) are suited at the 8b and 16c sites (colored purple) both connected to eight O atoms, whereas octahedral Zr occupies 16c sites (colored light blue). The red spheres correspond to oxygen atoms [13].

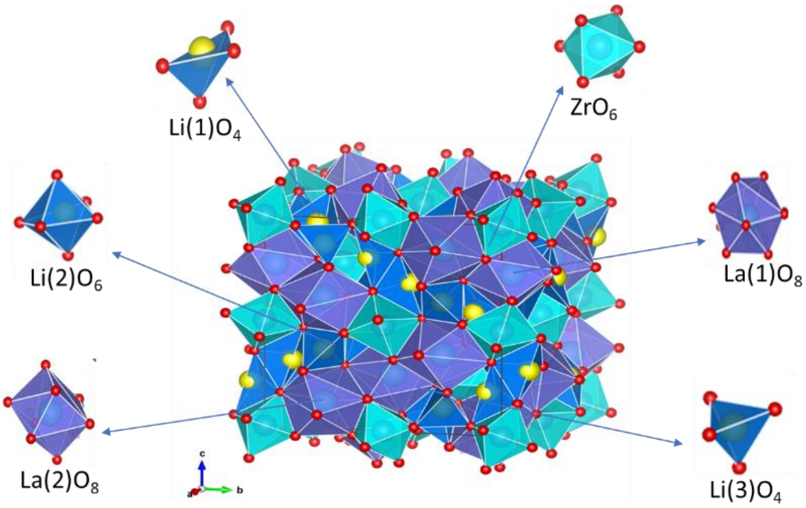

Figure 1.4: (a) Crystal structure of tetragonal $Li_7La_3Zr_2O_{12}$ (LLZO) with three Li coordination sites: tetrahedral Li(1) and octahedral Li(2) and Li(3).

The 8 per formula unit cell (pfu) tetragonal LLZO has 56 Li atoms, 24 La atoms, 16 Zr atoms, and 96 O atoms. The Wyckoff positions describe the sites of atoms in a crystal. Whereby a number and a letter denote the Wyckoff position. The number is the multiplicity of the site, and the letter is the Wyckoff site. Table 1.2 shows the position and equation of the arrangement of each atom in the crystal. The lithium atom is identified as Li(1), Li(2), and Li(3) since they occupy different Wyckoff positions, the same for La(1) and La(2). The zirconium atoms occupy the Wyckoff equation (0, 0, 0).

Table 1.1: Lattice parameters and volume of t-LLZO crystal structure.

	Lattice parameters			**Volume**
	a(Å)	b(Å)	c (Å)	V (Å^3)

$Li_7La_3Zr_2O_{12}$	13.12	13.12	12.67	2203

Table 1 2: Fractional coordinates, Wyckoff positions, and Wyckoff equations of sites occupied by constituent atoms of t-LLZO.

Atoms	Wyckoff Positions	Wyckoff equation	x	y	z
Li (1)	32g	x, y, z	0.917	0.586	0.694
Li (2)	16f	x, x + 1/4, 1/8	0.676	0.929	0.625
Li (3)	8a	0, 1/4, 3/8	0.5	0.75	0.875
La (1)	16e	x, 0, 1/4	0.628	0.5	0.75
La (2)	8b	0, 1/4, 1/8	0.5	0 .75	0.625
Zr	16c	0, 0, 0	0	0	0
O	32g	x, y, z	0.603	0.696	0.784

1.4 Rationale and Objectives

1.4.1 Rationale

Materials can undergo multiple doping to improve their properties, including electrical transport, mechanical properties, and photovoltaic performance. Pure LLZO can be stabilized by supervalent substitution at the Li, La, or Zr positions in LLZO [31]. Many metal elements have been employed to stabilize the cubic phase, among which Ga shows the most effective in enhancing the lithium-ion conductivity. More recently, Ga-doped LLZO (Ga-LLZO) ceramics with improved Li-ion conductivity higher than 1×10^{-3} S cm^{-1} are reported [32]. Of late, Shin et al. [27] reported that Ga and Ta could successfully stabilize the cubic phase and enhance the ionic conductivity simultaneously.

Supervalent dopants at the lithium sub-lattice are commonly used to stabilize the conductive cubic phase, through the creation of lithium vacancies. The use of germanium (Ge^{4+}) as a higher valent dopant substituting for Li^+ was studied and shown to stabilize cubic phase through substitution of x=0.10mol of Ge (at the tetrahedral 24d Li sites of the space group Ia3d, based on the neutron powder diffraction result) has been reported by Brugge et. al [33].

In order to further increase Li^+ conductivity of $Li_7La_3Zr_2O_{12}$, numerous studies on the chemical substitution using various cation species, such as Ta^{5+} [34], Ge^{4+} [35], Al^{3+} [36, 37], Ga^{3+} [38, 39], have been reported. Among them Ta substitution for Zr is highly appropriate due to three reasons [9]: (1) Ta is inert to metallic lithium; (2) it is able to stabilize the cubic garnet structure at a relative lower sintering temperature; (3) it can lower the lithium content, thus raising the lithium vacancy concentration, which is favorable for the enhancement of Li^+ conductivity. High ionic conductivity of $\sim 1\times10^{-3}$ $S.cm^{-1}$ has been achieved from Ta-substitution LLZO [40].

It is still anticipated that a more insightful study is necessary to improve LLZO with a higher ionic conductivity at room temperature and good phase stability, along with improving structural, mechanical, and electronic stability, and supervalent cation doping is considered the best strategy. The structural properties of material reflect the role of individual elements in the overall structure. It is important to determine the suitable cut-off energy and k-point mesh parameters for the t-LLZO structure and perform full geometry optimisation of the t-LLZO structures which allows the atoms in the system to relax and reach their ground-state energy level in that case the preferable host site for supervalent doping is identifiable, and the structural properties of the pure LLZO structure are analysed in terms of lattice parameters, the energy of formation and volume before introducing a dopant in the system. The electronic characteristics and mechanical strength of the material is evaluated in the form of electronic and elastic properties calculations.

In order to gain a fundamental understanding of the phase stability of Ta-doped LLZO and develop stable phases of Ta-doped LLZO with enhanced conductivity this work employs a Cluster Expansion (CE) method coupling framework with Density Functional Theory (DFT) for efficient and accurate energy evaluation through binary ground-state search using a genetic algorithm. The Monte Carlo simulation is utilised to gain insight into the behaviour of the Ta-doped phase as a function of temperature under a canonical ensemble. Consequently, further structural, mechanical, and electronic calculations are implemented on the generated structures to examine the effect of tantalum dopant.

1.4.2 Aims and objectives

The present study aims to perform detailed evaluation on the geometric optimization, structural, mechanical and electronic properties of pure tetragonal LLZO, and further introduce the tantalum (Ta) dopant on the optimized t-LLZO in order to enhance the conductivity of t-LLZO and develop new possible stable Ta-doped structures with optimized properties.

The objectives of this study will be to:

i. Determine the suitable cut-off energy and k-point mesh parameters for tetragonal LLZO structure, and perform full geometry optimisation of the t-LLZO structures
ii. determine the structural, electronic, and elastic properties of garnet-type t-LLZO solid-state electrolyte.
iii. Investigate the host site preference for supervalent doping.
iv. generate new stable Ta-doped structures using cluster expansion.
v. determine the thermal properties of the generated Ta-doped LLZO structures.
vi. evaluate temperature effect on the generated structures using Monte Carlo simulation.
vii. investigate the effect of tantalum to the system through mechanical property calculations.

1.5 Outline of the thesis

This dissertation gives a report on the study of the structural, mechanical, and electronic properties of pure and Ta-doped tetragonal LLZO oxide-garnet solid-state electrolyte, using the ab-initio method of DFT. Furthermore, phase properties of both pure and Ta-doped LLZO outline, using a combination of DFT, CE, and MC techniques.

The thesis is partitioned into five chapters: **chapter 1** deals with the historical overview based on theory and different techniques that have previously been used in the studies of these groups of oxide-garnet solid-state electrolytes. The crystal structure of the electrolyte is reviewed, and finally, the rationale, the aim, and the objectives are stated.

Chapter 2 is mainly about the methods that have been used in the current study: the DFT, CE, and Monte Carlo simulation methods. Firstly, the chapter introduces the first-principle techniques; secondly, the DFT method and the approximation functions used such as LDA and GGA are reviewed, followed by the VASP code. Then the CE along with the UNCLE code and the automatic ground-state search process are reviewed. Lastly, general technique information on the calculations properties such as the heat of formation, elastic constants, elastic modulus, band structure, and density of state.

Chapter 3 deals with the crystal structure relaxation and properties calculations: first, the convergence test is discussed in a form of cut-off energy and k-mesh point analysis, and then the structural properties of the crystal structure are analysed. The elastic properties are discussed in terms of elastic constants and elastic modulus analysis. Lastly, the electronic properties are analysed in terms of band structure and density of state.

Chapter 4 is mainly about the CE ground-state search for new structures and MC simulation: The binary ground state diagram generated by CE and the MC temperature profile are discussed and analysed in detail and then after, the structural, mechanical, and electronic properties results of the generated structures are discussed and analysed in detail.

Chapter 5 gives a summarised conclusion, recommendations for future research and a list of papers presented in conferences.
Finally, the bibliography, which helps give insight to the analysis of the work.

CHAPTER 2: Simulation applications and analysis.

Methodology

This chapter provides information on the calculation techniques used in this study. The computer simulation techniques offer an alternative way to analyse material properties (using computers), through which the simulator creates a prototype of a real system and investigates its behaviour. This approach has been widely used in solid state physics, chemistry and materials science, to predict the real situation by presenting physical systems as models. However, there is absolute control and access to details in a simulation, and given sufficient computational power, exact answers are discovered for the model.

High-performance computer techniques have enabled the modelling of solid-state electrolyte studies. The most well-known computing techniques are based on ab initio simulations [41]. Ab initio is a set of methods for determining the properties of materials, such as the values of fundamental constants and the atomic numbers of the atoms present, using Schrödinger equations. Density functional theory (DFT) and Hartree-Fock (HF) methods are examples of such techniques [42]. The current research will only focus on the concept of density functional theory.

Many variables have contributed to the current performance of ab initio calculations for real material structures. First, there is availability of modern high-speed computers. In interesting situations, this has made it possible to perform calculations on real materials with sufficient accuracy to allow meaningful detailed comparison with experimental measurements. The second is the emergence of density functional theory (DFT) and the continued development of approximations for electron exchange and comparison to the DFT formalism. The third is the development of the calculation techniques of band structure and the creation of ab initio pseudo-potentials [43], which contributed to the rapid estimation of total energies. Finally, significant new advances have occurred in the preparation of experimental techniques and materials that make it possible to check the structure of matter in ways that have never before been known. The ability to create high pressure and test the properties of matter over a wide range of densities is one advance. This is an excellent research method for providing information which can be directly compared with existing theoretical calculations.

2.1 Density functional theory

In the 1960s, Hohenberg and Kohn Sham [44] introduced Density Functional Theory (DFT) to provide the foundation for appropriate calculations. The Density Functional Theory (DFT) is a computational mechanical modelling method used to investigate the electronic structure of multi-body systems, especially atoms, molecules and condensed phases. DFT oxidizes the total density of electrons into one-electron densities

$$E = E[\rho] \tag{2-1}$$

which are integrated from wave functions of one-electron. The electron density in solid state systems, molecules and atoms is a scalar function determined in real space at each point r,

$$\rho = \rho(\boldsymbol{r}) \tag{2-2}$$

However, the density of the electron and the total energy depend on the atomic nuclei category and arrangements. Therefore, one can write

$$\mathrm{E} = \mathrm{E}[\rho(\mathrm{r}), \{\boldsymbol{R}_a\}] \tag{2-3}$$

where the set $\{R_a\}$ refers to the positions of all atoms, α, in the process under consideration. Equation (2-3) is essential for understanding the structural, mechanical, and electronic properties of matter on an atomic scale. In general, the derivative of total energy (2-3) in relation to the nuclear position of an atom gives the force acting on that atom. This makes it possible to search for stable structures efficiently and, perhaps more importantly, to study dynamic processes such as diffusion or molecular reaction on bulk structures. Most of the assumptions discussed here are based on the interpretation of the Born-Oppenheimer Approximation in which the electrons movements are infinitely slower than those of the nuclei. This implies that the electronic structure is determined for a given atomic configuration, and the atoms are then moved by classical mechanics. For heavy atoms such as tantalum (Ta), this is a good approximation, but may cause errors for light atoms such as lithium (Li).

In the density functional theory, the total energy (2-1) is decomposed into three contributions, a kinetic energy and a Coulomb energy due to electrostatic interactions between all charged particles in the process and a term called the energy of exchange-correlation capturing all multi-body interactions,

$$E = T_0 + U + E_{xc}. \tag{2-4}$$

The simplest word is the Coulomb energy U. It is essentially classic and includes the electrostatic energy from the attraction of Coulomb between electrons and nuclei, the repulsion between all electronic charges and the repulsion between nuclei

$$U = U_{en} + U_{ee} + U_{nn} \tag{2-5}$$

with

$$U_{en} = -e^2 \sum_{\alpha} Z_{\alpha} \int \frac{\rho(r)}{|r - R_{\alpha}|} dr \tag{2-6}$$

$$U_{ee} = e^2 \iint \frac{\rho(r)\rho(r')}{|r - r'|} dr dr' \tag{2-7}$$

$$U_{nn} = e^2 \sum_{\alpha\alpha'} \frac{Z_{\alpha} Z_{\alpha'}}{|R_{\alpha} - R_{\alpha'}|} \tag{2-8}$$

where e is a proton's elementary charge, and Z_{α} atomic number of atom α. The summations range in all atoms and all space integrations. Using the techniques of classical electrostatics, expression (2-6) to (2-8) can be evaluated once the electron density and the atomic numbers and positions of all atoms are understood.

The word kinetic energy, T_0, is more subtle. The "ordinary" electrons of a system are replaced in density functional theory by "efficient" electrons with the same distribution of charge, mass and weight. Active electrons, however, travel in an active potential as individual particles, while an "absolute" electron's motion is associated with all other electrons ' motion. T_0 is the sum of all active electrons ' kinetic energies traveling as individual particles. Sometimes, this distinction is not made explicitly between real and active electrons.

If a single particle wave function represents each effective electron, ψ_i, will provide the kinetic energy of all effective electrons in the system given by

$$T_0 = \sum n_i \int \psi_i^*(r) \left[-\frac{\hbar^2}{2m} \nabla^2 \right] \psi_i(r) dr \quad . \tag{2-9}$$

Expression (2-9) is the sum of one-particle kinetic energy expectations; refers to the number of electrons in state *i*. Complex correlations among the electrons are excluded from T_0 by construction.

The third term of Eq. (2-4), called exchange-correlation energy, E_{xc}, involves all remaining complicated electronic contributions to the total energy. The Hohenberg-Kohn-Sham theorem, which is a central part of DFT, states that total energy is constant with respect to the density of the ground state at its minimum value and that total energy is stationary with respect to density variations of the first order, i.e.

$$\frac{\partial E[\rho]}{\partial \rho}\Big|_{\rho=\rho_0} = 0 \qquad (2\text{-}10)$$

In tandem with the kinetic energy, one-particle wave functions $\psi_i(r)$ is introduced, which generate the electron density

$$\rho(r) = \sum_i n_i |\psi_i(r)|^2 \qquad (2\text{-}11)$$

Where n_i denotes the occupation number of the eigenstate *i*, which is represented by the one-particle wave function ψ_i. By construction, $\rho(r)$ in Eq. (2-11) is the exact many-electron density.

The goal of the next step is to derive equations that can be used for practical functional density calculations. The condition of variance (2-10) can be used to derive the conditions for the functions of one-particle wave leading to ground density. To this end, Eq. (2-11) is replaced by one in expression (2-10) and with respect to each wave function, the total energy varies. This technique results in the following formulas:

$$\left[-\frac{\hbar^2}{2m}\nabla^2 + V_{eff}(r)\right]\psi_i(r) = \varepsilon_i \psi_i(r) \qquad (2\text{-}12a)$$

With

$$V_{eff}(r) = V_C(r) + \mu_{xc}[\rho(r)] \qquad (2\text{-}12b)$$

Equations (2-12) are called the Kohn-Sham equations. The electron density, which corresponds to these wave functions, is the ground state density which minimizes the total energy.

Because of the partitioning of the total energy (2-4), the Hamiltonian operator in the Kohn-Sham equations (2-12) contains three terms, one for the kinetic energy, the second for the Coulomb potential and the third for the exchange-correlation potential.

The kinetic energy concept is the default second-order differential operator of Schrödinger equations with one-particle equations and its construction does not require specific device information, $V_C(r)$ and the exchange-correlation potential operator, μ_{xc} depend on the specific electron distribution in the system under consideration.

The Coulomb or electrostatic potential $V_C(r)$ at point r is generated from the electric charges of all nuclei and electrons in the system. It can be evaluated directly in a real space,

$$V_C(r) = -e^2 \sum_\alpha \frac{Z_\alpha}{|r - R_\alpha|} + e^2 \int \frac{\rho(r')}{|r - r'|} dr' \tag{2-13}$$

In condensed systems it is more convenient to use Poisson's equation

$$\nabla^2 V_C(r) = -4\pi e^2 q(r) \tag{2-14}$$

To estimate the potential of electrostatics. Here, $q(r)$ denotes both the electronic charge distribution $\rho(r)$ and the positive point charges of the nuclei at positions R_α.

The exchange-correlation potential is related to the exchange-correlation energy by

$$\mu_{xc}(r) = \frac{\partial E_{xc}[\rho(r)]}{\partial \rho(r)} \tag{2-15}$$

Equation (2-15) is theoretically correct in the sense that the full multi-body interactions are not approximated.

The total energy functional of Kohn-Sham can be expressed as

$$E = \frac{1}{2}\sum_{occ} \varepsilon_i + U_{nn} - \frac{e^2}{2}\iint \frac{\rho(r)\rho(r')}{|r - r'|} dr dr' + E_{xc}[\rho(r)] - \int \rho(r)\mu_{xc} dr \tag{2-16}$$

2.2 Local density approximation

Local density approximations (LDA) sets of approximations to the E_{XC} functional in DFT are determined by the electronic density at each point in space. The LDA shows that E_{XC} is like a locally uniform electron gas of similar density in regions where load density varies slowly [45]. The approximation is used where the E_{XC} density is locally of an inhomogeneous system substituted by that of an electron gas evaluated at local density. LDA is based on two basic assumptions: first that the effects of exchange and correlation are mainly from the immediate region of point r, and second that these effects of exchange and correlation are partially independent of varying the concentration of electrons in the region r [46].The completion of these two conditions results in the same volume component contribution ***dr*** as if this volume element was surrounded by a constant electron density *p*(*r*) of the same value as within ***dr***. In this approximation, the exchange-correlation energy density of the homogeneous electron gas $E_{XC}^{hom}(\rho_0)$ dependent on the homogeneous density ρ_0 and replaces this for the inhomogeneous system with density ρ(r) by

$$E_{XC}^{LDA}\big(\rho(r)\big) = E_{XC}^{hom}(\rho_0)|_{\rho_0}, \qquad (2\text{-}17)$$

A local density approximation for the exchange-correlation energy is written for spin-unpolarised system (where the functional depends only on frequency)

$$E_{XC}^{LDA}[\rho] = \int p(r)\mathcal{E}_{XC}(\rho)dr, \qquad (2\text{-}18)$$

and

$$\frac{\delta E_{XC}(\rho(r))}{\delta\rho(r)} = \frac{\partial[\rho(r)\mathcal{E}_{XC}(r)}{\partial\rho(r)}, \qquad (2\text{-}19)$$

ρ is the electronic density and E_{XC} the exchange-correlation energy density. We get a more detailed look at LDA when we consider the xc-hole and the pair correlation function.

$$\rho_{XC}^{LDA}(r_1, r_2) = \rho(r_1)[g^{hom}([\rho]; |r_1 - r_2|], \qquad (2\text{-}20)$$

Where $g^{hom}[\rho]$ the pair-correlation function of the homogeneous electron gas is constantly integrated [47]. The part of the pair correlation exchange-correlation function that is not affected by the constant integration of the coupling is given by;

$$g_{xc}^{LDA}([\rho];\ r_1, r_2) = 1 - \frac{9}{2}\left[\frac{sin(k_F(r_1)|r_1-r_2|-k_F(r_1)|r_1-r_2|cos((k_F(r_1)|r_1-r_2|)}{(k_F(r_1)|r_1-r_2|)^3}\right]^2 \qquad (2\text{-}21)$$

where $k_F(r)$ the local vector of the Fermi wave is defined as:

$$k_F(r) = (\frac{3}{\pi})^{\frac{1}{3}}\rho(r)^{\frac{1}{3}} \qquad (2\text{-}22)$$

The exchange-correlation energy is decomposed into exchange and correlation terms linearly

$$E_{XC} = E_X + E_C, \qquad (2\text{-}23)$$

So that separate expressions for E_x and E_c are sought. The exchange term takes on an analytic form for the homogeneous electron gas (HEG). This expression is used by the LDA for exchange under the assumption that the exchange-energy in a system where the density is non-homogeneous is obtained by applying the results of the HEG point wise, giving the expression [48] [49].

$$E_x^{LDA}[\rho] = -\frac{3}{4}(\frac{3}{\pi})^{\frac{1}{3}}\int \rho(r)^{\frac{4}{3}}dr, \qquad (2\text{-}24)$$

The appropriate exchange scaling is satisfied with this formula. There are corresponding equations for the correlation part of of $[\rho]$ and for $E_C^{LDA}[\rho]$. The LDA xc-hole is spherical around the reference electron

$$\rho_{XC}^{LDA}(r_1, r_2) = \rho_{XC}(r_1, s), \qquad (2\text{-}25)$$

where $s = |r_1 - r_2|$ and it also satisfies the sum rule,

$$\int \rho_{XC}^{LDA}(r_1, r_2) dr_2 = 4r \int_0^{\infty} \rho_{XC}^{LDA}(r_1, s)\, s^2 ds = -1, \qquad (2\text{-}26)$$

Except in the high-density and low-density limits corresponding to infinitely weak and infinitely strong correlation, analytical expressions for the HEG correlation energy are not known. For a HEG with density ρ, the high-density limit of the energy density of the relation is [48]

$$\varepsilon_0 = Aln(r_s) + B + r_s(Cln(r_s) + D), \qquad (2\text{-}27)$$

and the low limit

$$\varepsilon_0 = \frac{1}{2}(\frac{g_0}{r_s} + \frac{g_1}{r_s^{\frac{3}{2}}} + \ldots ...., \qquad (2\text{-}28)$$

Where the radius of Wigner-Seitz is related to the density as

$$\frac{4}{3}\pi r_s^3 = \frac{1}{\rho}, \qquad (2\text{-}29)$$

Local-density approximations are critical for the construction of more sophisticated approximations of exchange-correlation power, such as generalized gradient approximations or hybrid functionality, as the desirable property of any approximate exchange-correlation functionality is that it reproduces the exact results of homogeneous electron gas (HEG) for non-variant densities. Therefore, LDA's are often an explicit component of such functional.

2.3 Generalized gradient approximation

Perdew [50], Becke [51], and Ernzerhof [52] proposed the generalized gradient approximations (GGA) for the exchange-correlation energy, which improve on the local spin density (LSD) description of atoms, molecules, and solids discussed above. LDA approximates the true density's energy by the energy of a local constant density and fails in situations where the density changes rapidly, such as in molecules. The basic idea behind gradient-corrected density functional is to include terms in exchange-correlation expressions that depend on the gradient of the electron density at each point in space rather than just its value. The GGA exchange-correlation energy functional can be expressed as

$$E_{XC} = E_{XC}[\rho(r), \nabla \rho(r)] \ , \qquad (2\text{-}30)$$

which improves on the LDA results and is superior to correlated wave-function methods. In comparison to the LDA, GGA provides distinct parameterisations. As a result, the GGA with gradient-corrected functional is denoted as

$$E_{XC}^{GGA}[\rho_{\uparrow,}\ \rho_{\downarrow}] = \int d^3rf(\rho_{\uparrow}(r), \rho_{\downarrow}(r), \nabla\rho_{\uparrow}, \nabla\rho_{\downarrow})\ , \tag{2-31}$$

This expression reduces LSD atomization energy errors by about a factor of 5. The Becke GGA [51] for exchange energy and the exchange and correlation GGAs by Perdew and Wang [50] are the most commonly used GGAs. The Becke GGA correlation to the LDA is presented in the following form:

$$E_{x}^{GGA}[\rho_{\uparrow}, \rho_{\downarrow}] = E_{X}^{LDA} - \beta \int \sum_{\sigma} \frac{\rho_{\sigma}(r)^{\frac{4}{3}} x_{\sigma}^{2}}{1+6\beta x_{\sigma} \sinh^{-1} x_{\sigma}} d^3r, \tag{2-32}$$

and

$$E_{X}^{LDA} = -C_{X\sigma} \sum \rho_{\sigma}^{\frac{4}{3}}(r) d^3(r)\ , \tag{2-33}$$

where $C_X = \frac{3}{2}\left(\frac{3}{4\pi}\right)$, $X_{\sigma} = \frac{|\nabla\rho|}{\rho_{\sigma}^{\frac{4}{3}}}$ and σ denotes electron spins, which can be spin-up (↑) or spin-down (↓). The constant (β) is a parameter used to calculate the nobble gas exchange energy.

2.4 VASP code

Vienna ab initio simulation package computer program that is used to model atomic-scale materials from first principles, such as electronic structure calculations and quantum-mechanical molecular dynamics. VASP solves the Kohn-Sham equations by computing an approximate solution to the many-body Schrödinger equation within density functional theory (DFT). Central quantities such as one-electron orbitals, electronic charge density, and local potential are expressed in plane-wave basis sets in VASP [41]. The projector-augmented-wave method is used to describe electron-ion interactions. For transition metals and first row elements like Li and O, the PAW method allows for a significant reduction in the number of plane waves per atom. In general, bulk materials require no more than 100 plane waves (PW) per atom; in most cases, even 50 PW per atom will suffice for a reliable description.

VASP can calculate forces and the full stress tensor, which can then be used to relax atoms into their instantaneous ground state. It employs efficient iterative matrix diagonalization techniques, such as the residual minimization method with direct inversion of the iterative subspace (RMM-DIIS) or blocked Davidson algorithms, to determine the electronic ground-state. To speed up the self-consistency cycle, these are coupled to highly efficient Broyden and Pulay density mixing schemes. VASP includes a full-featured symmetry code that automatically determines the symmetry of arbitrary configurations. The symmetry code is also used to create the Monkhorst Pack special points, which allows for the efficient calculation of bulk materials and symmetric clusters. The Methfessel-Paxton smearing and tetrahedron methods are used to integrate the band-structure energy over the Brillouin zone. Blöchl's corrections, which remove the quadratic error of the linear tetrahedron method, is used for the tetrahedron method, resulting in a fast convergence speed.

2.5 The cluster expansion

Mayer proposed cluster expansion as an approximate computation method in 1941 [53]. Cluster expansion is a pipelining computation method commonly used in computational materials science to approximate material properties (e.g., to combine first-principles calculation and Monte Carlo simulation). Predicting and describing the crystal structure of materials has long been a challenge for materials researchers and developers. Before the nineteenth century, the primary approach was experimental research, even if the majority of it was based on guesswork. It can take months to develop new material, and there is a lot of trial and error involved [54]. As a result, quantitative approaches to materials research have evolved into an indispensable tool for systematic research. A direct relationship exists between the function or property of a material and its fundamental descriptors (e.g. the electronic conductivity of a material can be traced back to the properties and arrangements of the elements of which it is composed) [55]. Cluster expansion enables the total energy calculation of a crystal structure with a mass of atoms and expresses the partition function as a series of expansions in powers of density [56]. Using cluster structure formation as a parameter, the general basic principle of cluster expansion energy parameterization is described below.

2.5.1 Basic principle of the cluster expansion

The cluster expansion's core concept is to express the scalar physical quantity of material, $q(\sigma)$, to its configuration, σ, where a crystalline system is represented by a fixed underlying grid of atomic sites. Any configuration with the same underlying topology can be completely specified by the atomic occupation of each atomic site in such a representation. Although the basic CE framework can be extended to multicomponent systems, the focus of this study is on binary systems. As a result, a cluster is considered (basic lattice), which is made up of two types of atoms, A and B. The spin variable q, which has the value +1 if atom A sits on-site q or -1 if atom B sits on q, determines the type of atom at point q in the cluster. Three configurations are shown in figure 2.1 as an example and labelled based on the assignment of the spin variable.

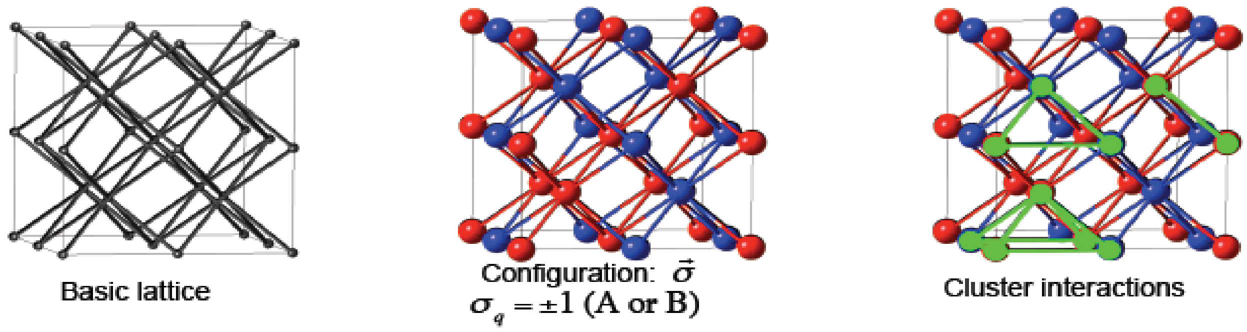

Figure 2.1: The diagram is decomposed into a set of truncating structures and clusters.

An expansion of cluster interactions and their respective interaction energies J can define the energy (σ) associated with structure by means of equation

$$E(\vec{\sigma}) = J_0 + J_1 \sum_i \sigma_i + \sum_{i>j} J_{ij}\sigma_i\sigma_j + \sum_{i>j>k} J_{ijk}\sigma_i\sigma_j\sigma_k + \cdots \tag{2-34}$$

A constant, configuration-independent contribution is represented in this formula J_0, the first term. The second term is concentration-dependent and is a sum of on-site energy J_1 times the pseudo-spin operator σ at each site i over all N sites of structure. Other terms characterize cluster interactions between multiple sites, such as J_{ij} two-body interactions or J_{ijk} three-body interactions. The spin products $\sigma_i\sigma_j$... are included over all f vertices of the cluster times its active cluster interaction energy J_{ij}... summed up in all possible ways that the cluster can be put on the lattice of the structure σ. In other words, the energy (σ) of the σ system is broken down into clusters with their corresponding active interaction energies. Cluster expansion's core issue is to define a universal set of best-suited J interactions to represent a given system. It is useful to reformulate the above equation in a more compact form to achieve this,

$$E(\vec{\sigma}) = \sum_{C \epsilon \vec{C}} J_C \Pi_C(\vec{\sigma}) \tag{2-35}$$

The cluster expansion formula summarizes the J_C interaction energy product of cluster C's with its correlation variable,

$$\Pi_C(\vec{\sigma}) = N^{-1} \sum_{i=1}^{N} \sum_{k \in C} \prod_{\nu \epsilon \vec{f}} \sigma_\nu \tag{2-36}$$

A sum can be placed on the N sites of the structure in all possible ways in which a cluster C with $\vec{f}$ vertices can be placed. In the correlation function, the spin product $\sigma_1 \ldots \sigma_f$ goes beyond the cluster's f vertices. Also, symmetry inequivalent clusters are now being considered and the vector $C = \{C_1, \ldots, C_n\}$ will capture clusters included in an expansion.

2.5.2 UNCLE code

Cluster expansion calculations were performed using the Universal Cluster-Expansion (UNCLE) code [57] developed by the group of S. Muller, at Harburg-Hamburg University of Technology. The implementation of UNCLE code is applicable to as many systems as possible, i.e. arbitrary lattices and multi-component systems. The code simplifies the interaction between the cluster expansion and common DFT codes. Using a genetic algorithm, the code contains efficient tools for the use of effective cluster interactions (ECIs), such as in kinetic or thermodynamic Monte Carlo simulation or ground state searches. Simulations for Monte Carlo are implemented to obtain results for temperatures T=0. It takes account of configuration entropies. The choice of atomic configurations, from which the ECIs are extracted, affects the ECIs. To avoid biasing the input database, and thus the ECIs, we systematically increase the database. We begin with a hand-chosen set {σ} of usual suspects, small-unit-cell structures derived from the parent lattice, and some quasi-random structures. The first cluster expansion determined from this initial set makes predictions, perhaps not accurately, for the ground states and other structures with enthalpies of the formation near the convex hull. These predictions are in turn calculated via first principles and added to the input database. This cycle is repeated, as shown in figure 2.2, letting the current cluster expansion itself pick new structures to add to the database.

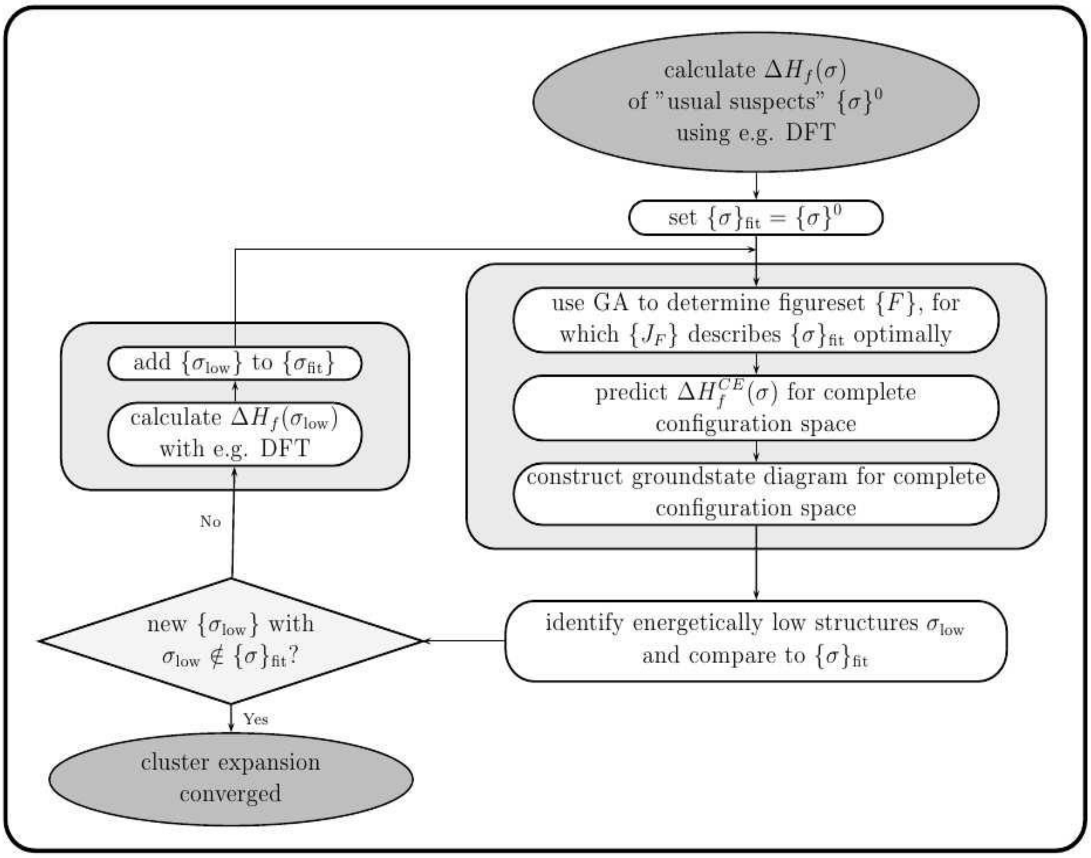

Figure 2.2: Self-consistent working plan as used by UNCLE for the cluster expansion to find new input structures [57].

2.5.3 Genetic algorithm

A generic algorithm (GA) is a computational model based on Darwin's theory of biological evolution. It searches for optimal solutions by simulating natural evolutionary processes [58]. For GA to work in practice, one starts with a set of candidate solutions, i.e., the atomic structures in the present study. These first-generation structures can be generated either randomly or with some constraints. Only individuals with a better fitness level will survive and be selected to form the next generation based on their fitness level. Inversion, crossover, and mutation are operators used for generating the new generations. The evolution process will be repeated until the pre-set criteria are reached. The genetic algorithm covers the traditional CE (called iter1 in the present work) which can deal with different concentrations using a small cell and meanwhile includes searching using a larger super-cell, which enables a more thorough search.

2.5.4 Selecting the Input Structures

A very important task of the convergent CE is to ensure that the data and the corresponding active interaction energies chosen are not prejudiced by the training set. UNCLE uses the chosen figure set to match the energy of other systems to avoid a misinterpretation of the entire system by choosing the wrong input. New structures can now be constructed and, if they lie energetically below the current ground state line, are recalculated by DFT, providing a new collection of input structures. Then a new set of figures is put in place and the procedure is repeated. Such an iterative approach has the advantage that a consistent ground-level line can be achieved together with a figure set that produces accurate results.

2.5.5 Automatic ground-state search

In order to search for the ground state clusters and further determine the temperature effect on the system, the UNCLE code implements a genetic algorithm to identify an optimum set of clusters with their corresponding interaction parameters derived from the energies of structures contained in a training set. The energies of the structures contained in the training set are calculated using a DFT method.

The structures are chosen using the CE flowchart settings listed below: In the UNCLE control settings, first, choose the CE with GGA flowchart, then the optimize cluster expansion option. The type of cluster expansion in bulk and the maximum number of unit cells is set to one in the control setting. The genetic algorithm is the algorithm for fitting the cluster expansion. The maximum number of structures added in each iteration for iterative optimization parameters is 20. The number of structures to initialize the first iteration is 20, and the optimization is set for a maximum of 30 iterations. The miscibility of constituent is set at automatic mode, for the CE to automatically indicate whether the system is a miscible constituent or miscibility gap. For the convergence criterion, 5meV/position is set for CE optimization, and 10 clusters were used to assess the quality. The CE was set to run different structures simultaneously.

The effective structures are iteratively added to the training set during the fitting procedure as shown in figure 2.3 below. Convergence is achieved when no new ground-state structures are found by CE. From the converged CE, a set of effective cluster interactions is extracted and used in large-scale Monte Carlo simulation to explore order-disorder phenomena and phase separation process as a function of temperature.

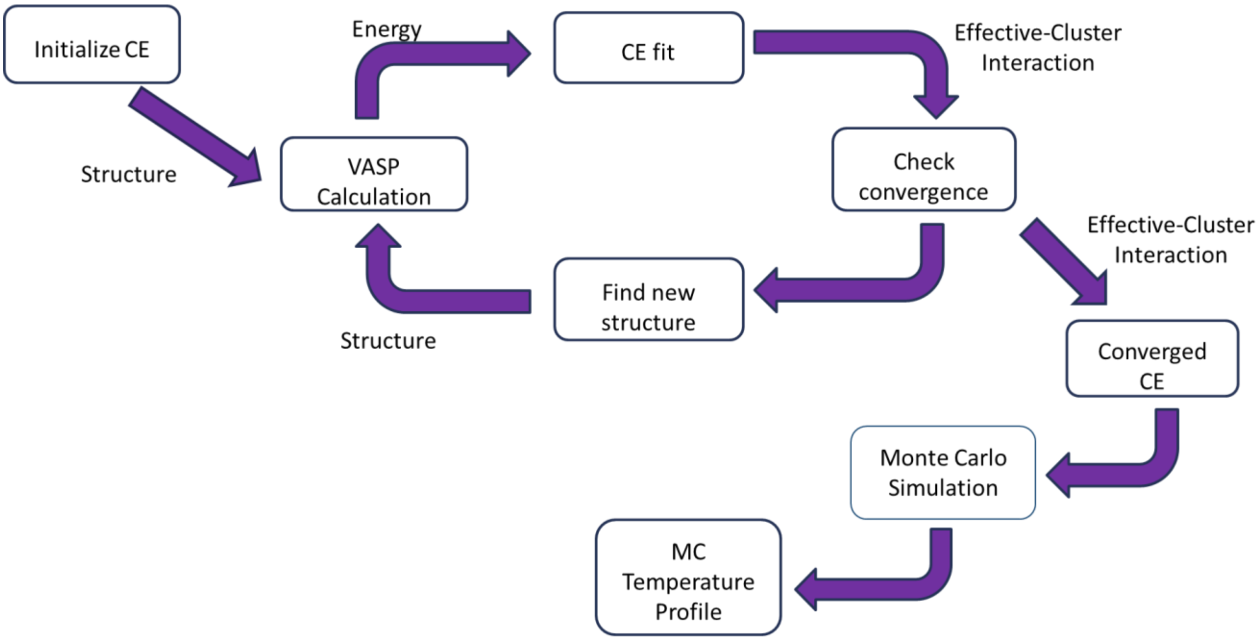

Figure 2.3: Illustration of cluster expansion automatic ground state search

2.6 Monte Carlo simulation

Monte Carlo Simulations are mathematical models that generate random variables to depict the risk or uncertainty related to a certain system. This is a method common in statistics and thermodynamics [59]. Random variables or inputs are modelled using probability distributions like normal, log normal, and so on. For generating paths, various iterations of simulations are run, and the outcome is determined using appropriate numerical computations. The primary applications are integral estimation, mean value calculation, and the search for global minima in phase space. A set of effective cluster interactions can be extracted from an optimized cluster expansion and used in large-scale Monte Carlo simulations to study order-disorder phenomena and phase segregation processes as a function of temperature. To obtain results for temperatures T=0, Monte Carlo simulations are implemented.

2.6.1 Random Walks and Markov-chains

As mentioned before, the selection of the sample is the crucial point in finding the investigated system's thermodynamic characteristics. The crucial question is, what happens to the jump from one point to the next? MC uses a random method to change the point in the phase space: the point has the same probability of being chosen as the next one to be considered by applying the so-called random walk strategy. The corresponding transformation probability P now depends only on the phase space current point, but not on the previously selected n-2 points. This transition probability description is referred to as a Markov chain.

$$\mathrm{P}(\ \mathrm{k_n} = i|K_{n-1} = j| \dots\dots |K_0 = l) = P(K_n = i|K_{n-1} = j) = P_{ij}(n) \qquad (2\text{-}37)$$

Assuming that each probability of transition P can be written as $P_{ij}(n)$ a matrix containing the transition to each phase space point can be described as Z.

$$\mathrm{P} = \begin{pmatrix} P_{11} & \cdots & P_{1K} \\ P_{12} & \cdots & P_{2K} \\ \vdots & \ddots & \vdots \\ P_{K1} & \cdots & P_{KK} \end{pmatrix} \qquad (2\text{-}38)$$

2.6.2 Canonical ensemble

The maintained quantity in a canonical ensemble is the concentration of each form of atom in the simulation container. The location of the two randomly selected atoms is exchanged in each step. This makes it possible to write the energy of the composition in the box and the rate of change as

$$P^*_{\sigma\sigma'} = \begin{Bmatrix} 1 & if\ \epsilon < e^{-(E(\sigma')-(E(\sigma))/kT} \\ 0 & f\ \epsilon > e^{-(E(\sigma')-(E(\sigma))/kT} \end{Bmatrix} \qquad (2\text{-}39)$$

The random walk through phase space is continued until a defined number of steps are completed or the change in the system's energy is below a specified number limit.

2.7 Theoretical back-ground of calculations properties

Theoretical and computational analysis facilitates in comprehending the relationship between material composition, structure, and behaviour. The development and application of computational tools based on physical and chemical principles help to generate "working equations" that can be solved using a computer. The study is based on theories of quantum mechanics. It is possible to save time and expenses on laboratory experiments by using computational tools, as well as to understand experimental processes in greater depth. Structure, mechanical, and electronic properties of materials can all be observed using simulation. This is to gain a thorough understanding of the atomic factors that influence material properties, improve material functionality, and even develop innovative, more efficient materials.

2.7.1 Cut-off energy

The cut-off point is referred to as the plane wave kinetic energy cut-off, it is greater than or equal to the highest kinetic energy of the plane waves used. In general, the cut-off energy must be chosen according to the pseudo-potential. The cut-off energy tells us about the cut-off on the number of plane wave functions being utilized as basic functions to represent the wave function. Theoretically, an infinite number of basic functions is required to produce an exact answer. The energy cut-off for planewave systems is usually tested by examining the convergence of energy differences between two like-systems. An increase in cut-off energy will increase the number of planewaves, which will increase the accuracy of the description of the ion cores. As long as an increase in the number of planewaves does not increase the charge density in the bonding region, an additional number of planewaves increases the energy per atom of the systems by a constant amount, hence the energy differences remain the same.

2.7.2 K-sampling

The k-sampling is used to specify the Bloch vectors (k-points) that will be used to sample the Brillouin zone in electronic calculations. For a periodic system, the k points appearing in the wave function belong to the first Brillouin zone, by virtue of the Bloch's theorem. In the case of samples with defects, which are by definition aperiodic, the cell that contains the defects is periodically repeated, using periodic boundaries. The Blöch theorem can be therefore applied to this super-cell, the dimension of the Brillouin zone being determined by the dimension of the super-cell itself, i.e. the larger the super-cell, the smaller the Brillouin zone should be.

The k-points at which the Brillouin zone is to be sampled during a self-consistent calculation to find the electronic ground state may be defined either by specifying a list of k-points or a Monkhorst-Pack grid in terms of the dimensions of the k-point mesh or a minimum k-point density [60]. The origin of the Monkhorst-Pack grid may be offset by a vector from the origin of the Brillouin zone. The k-points list:

$$\begin{array}{cccc} R_{1i} & R_{1j} & R_{1k} & R_{1\omega} \\ R_{2i} & R_{2j} & R_{2k} & R_{1\omega} \end{array} \qquad (2\text{-}40)$$

The first three entries on a line are the fractional positions of the k-point relative to the reciprocal space lattice vectors. The final entry on a line is the weight of the k-point relative to the others specified. The sum of the weights must be equal to 1. The k-points Monkhorst-pack grid:”

$$I_i \quad I_j \quad I_k \qquad (2\text{-}41)$$

The number of k points needed for a calculation depends critically on the necessary precision and on whether the system is metallic. Insulating systems require an order of magnitude less k points than semiconducting and metallic systems [60]. The number of k points also depends on the smearing method in use; not all methods converge with similar speed. Therefore, absolute convergence with respect to the number of k points is necessary.

2.7.3 Geometry optimization

Geometry optimization, or the relaxation of atomic positions and cell parameters, is performed prior to any calculations. The first step in geometry optimization will typically have the most self-consistent functional (SCF) iterations. When performing a full optimization of atomic positions and cell shape/volume, it is almost always best to do so in stages. Finding the ground-state of a system in which the ions and electrons have the lowest energy configuration is a simple matter of geometry optimization. Following a shift in the atomic positions, the SCF iterations are repeated. The convergence criteria for the electronic ground-state continue to apply per SCF iteration, as do the convergence criteria for the geometry per SCF cycle, which are often energy and force tolerances.

The Hellman-Feynman (H-F) Force Theorem provides the directional guide for the change in ionic positions and the calculated force on the nuclei [61]. The force on an ion is given by the derivative of the total energy with respect to the position of the ion i.e.

$$F_I = -\frac{dE}{dR_I} \tag{2-42}$$

Providing the wave-function are eigenstates of the Kohn-Sham Hamiltonian, i.e.

$$F_I = -\frac{\partial E}{\partial R_I} - \sum_i \frac{\partial E}{\partial \varphi_i^*}\frac{d\varphi_i^*}{dR_I} \tag{2-43}$$

The electronic structure is relaxed to its ground-state in a fixed ionic configuration, where the φ_i are the eigenstates, and then the forces on the ions are calculated. The ions are then moved in the direction of the H-F forces, and the electronic structure is relaxed to its ground-state for the new configuration, starting off the new SCF cycle with the wave functions obtained from the previous ionic configuration. This cycle is repeated until all atoms' residual forces are less than a specified tolerance. Forces are more difficult to calculate accurately than energies, which are sensitive to second-order errors in φ_i because they are sensitive to first-order errors in φ_i. As a result, the force convergence criteria used in ceramic materials research are four orders of magnitude greater than those used for electronic structure energy convergence and three orders of magnitude greater than those used for geometry energy tolerance.

2.7.4 Heats of formation

The standard enthalpy of formation or standard heat of formation of a compound is the change of enthalpy that accompanies the formation of 1 mole of a substance in its standard state from its constituent elements in their standard states (the most stable form of the element at 1 bar of pressure and the specified temperature, usually 298.15 K or 25 degrees Celsius). Its symbol is ΔH_f. The heats of formation and associated entropies provide a fundamental understanding on stabilities and phase diagrams construction. The heat of formation is estimated by

$$\Delta H_f = E_c - \sum_i x_i E_i \qquad (2\text{-}44)$$

where E_c is the calculated total energy of the compound, E_i is the calculated total energy of the element i in the compound [62].

In the present work, formation energy is calculated to evaluate the relative stability of different structures, which is defined as:

$$E_f = \frac{E_t}{N_{site} \, X \, N_{size}} - \sum_n c_n e_n^{ref} \qquad (2\text{-}45)$$

where E_f, E_t and e_n^{ref} are formation energy, total energy and reference energy of the element n, respectively. N_{site} and N_{size} are the number of site i in the primitive cell and the number of primitive cell contained in a super-cell, and c_n is the concentration of the element n. Formation energy from DFT and CE calculations are both based on this equation.

2.7.5 Elastic constants

Elastic constants measure the proportionality of strain and stress in a crystal, provided that the strain is not so great that Hook's law is violated. Applying a strain to a crystal, measuring the energy versus strain, and calculating the elastic constant from the curvature of this function at zero strain is how the elastic constant is computed. A certain linear combination of elastic constants is associated with a given strain. C_{11}, C_{12}, C_{13}, C_{16}, C_{33}, C_{44}, and C_{66} are the three independent elastic constants for tetragonal systems. The elastic constants are defined as the second derivative of the Gibbs free energy as a function of strain, i.e.

$$C_{ij} = \frac{1}{V_0}\left(\frac{\partial^2 E}{\partial \varepsilon_i \, \partial \varepsilon_j}\right) \qquad (2\text{-}46)$$

where C_{ij} is the tensor of elastic constants, V_0 is the crystal volume, the Einstein summation rule over the repeated subscripts is implied, and Voigt's strain notation is used Harmonic approximation is the term used to describe the quadratic dependence of elastic energy on strains. The symmetry of the crystal determines the total number of independent components of the elastic constant tensor.

2.7.6 Elastic stability criteria

For each material, both stress and strain have three tensile and shear components, giving six components in total. For each material, both stress and strain have three tensile and three shear components, giving six components in total According to the theory of elasticity, a 6×6 symmetry matrix with 36 elements is needed to describe the relationship between stress and strain, such that $\sigma_1 = C_{ij}\varepsilon_j$ for small stresses, σ and strain, ε. Therefore, the strain dependence of stress can be expressed as

$$\begin{pmatrix} \sigma_x \\ \sigma_y \\ \sigma_z \\ \tau_{yz} \\ \tau_{xz} \\ \tau_{xy} \end{pmatrix} = \begin{pmatrix} C_{11} & C_{12} & C_{13} & 0 & 0 & 0 \\ C_{12} & C_{11} & C_{13} & 0 & 0 & 0 \\ C_{13} & C_{13} & C_{33} & 0 & 0 & 0 \\ 0 & 0 & 0 & C_{44} & 0 & 0 \\ 0 & 0 & 0 & 0 & C_{44} & 0 \\ 0 & 0 & 0 & 0 & 0 & C_{66} \end{pmatrix} \times \begin{pmatrix} \varepsilon_{xx} \\ \varepsilon_{yy} \\ \varepsilon_{zz} \\ \gamma_{yz} \\ \gamma_{xz} \\ \gamma_{xy} \end{pmatrix} \tag{2-47}$$

Where σ and τ represent tensile and shear stress while ε and γ represent tensile and shear strain, respectively [63].

Basically, elastic constants of a material describe its response to the external applied strain or the stress required to maintain. a given deformation and provides useful information of the strength of the material, as characterized by Bulk modulus (*B*), shear modulus (*G*), Young's modulus (*E*), Poisson's ratio (v) and Shear anisotropy factor (*A*). Quadratic dependence of the crystal energy *E* on the strain is expected for small deformations. The elastic moduli for tetragonal crystal are given as follow [64]:

$B = \frac{1}{9}\left(2C_{11} + C_{33} + 4C_{13} + 2C_{12}\right)$ $\quad$ $G = \frac{1}{15}\left(2C_{11} + C_{33} - C_{12} - 2C_{13} + 6C_{44} + 3C_{66}\right)$

$E = C_{33} - 2vC_{13}$ and $v = \frac{C_{13}}{C_{11} + C_{12}}$

The corresponding necessary conditions for mechanical stability criterion are [65]:

$$C_{44} > 0,\ \ C_{66} > 0,\quad C_{11} > 0,\ C_{33} > 0, C_{11} - C_{12} > 0,\quad (C_{11} + C_{33} - 2C_{13}) > 0,$$

$$(2C_{11} + C_{33} + 2C_{12} + 4C_{13}) > 0$$

In metals (a partial or complete solid solution of one or more elements in a metallic matrix) behaving like isotropic media, the young's modulus is proportional to the bulk modulus when the poison's ratio is close to 1/3.

2.7.7 Band structure

The band structure of a solid in solid-state physics describes the ranges of energy, called energy bands, that an electron within the solid may have and ranges of energy, called band gaps, which it may not have. Band theory, which models the behaviour of electrons in solids, postulates the existence of energy bands. It is successful in explaining the many physical properties of solids using the band structure of a material. Bands can also be thought of as the large-scale limit of the molecular orbital theory.

The electrons in an isolated atom are arranged in atomic orbitals, which are discrete energy levels. In a molecule, the atomic orbitals of two or more atoms are separated into distinct molecular orbitals, each with a different energy level. Due to this, a number of molecular orbitals are formed in proportion to the number of valence electrons. As atoms combine into solids, the number of orbitals increases dramatically. As a result, their differences in energy are extremely small. Moreover, the energy levels of solids form continuous bands of energy rather than discrete levels. The absence of orbitals in some energy intervals, however, results in band gaps. This concept is especially important in the context of semiconductors and insulators.

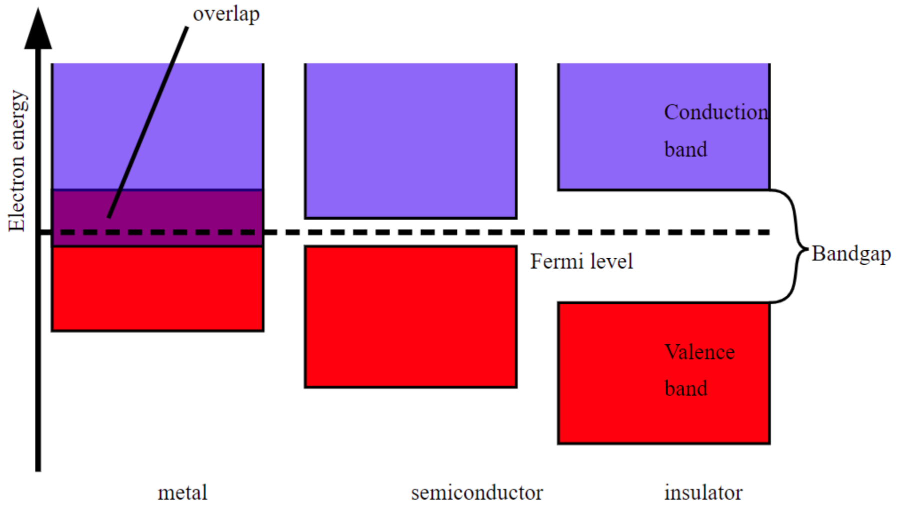

Figure 2.4: A band gap diagram showing the different sizes of band gaps for metals, semiconductors, and insulators [66].

As shown on the left, a conductor (here representing a metal) has its empty and filled bands overlapping, allowing exciting electrons to flow through the empty band without much force. Due to their large energetic differences between the valence band and the conduction band, semiconductors and insulators require a higher voltage to conduct electrons.

2.7.8 Density of State

The density of states (DOS) of a system describes the number of states per interval of energy at each energy level that are available. The DOS indicates how densely packed quantum states are in a system. Integration of DOS over a range of energy yields a number of states;

$$\mathrm{N(E)} = \int_{\mathrm{E}}^{\Delta\mathrm{E}} \mathrm{g(E)dE} \qquad (2\text{-}48)$$

where N(E) denotes the carrier density and g(E)dE represents the number of states between E and dE. The density of states permits integration to be done with respect to the electron energy instead of the integration over the Brillouin zone. It is often used for quick visual analysis of the electronic structure. Characteristics such as the width of the valence band, the energy gap in insulators, and the intensity of the main features are helpful in interpreting experimental spectroscopic data. The most accurate methods used are based on linear or quadratic interpolations of band energies between the reference points in the Brillouin zone. The most popular and reliable technique is based on tetrahedron interpolation. However, it is not well suited to the Monkhorst-Pack grid of special points which the VASP code uses a simplified linear interpolation scheme. The method is based on linear interpolation in parallelepipeds formed by the points of the Monkhorst-Pack set, which is followed by the histogram sampling of the resultant set of band energies.

CHAPTER 3: First-Principles Study on Structural, Mechanical and Electronic Properties of $Li_7La_3Zr_2O_{12}$ (LLZO) Solid Electrolyte.

3.1 Introduction

In this chapter, the DFT results performed on the tetragonal $Li_7La_3Zr_2O_{12}$ (LLZO) oxide garnet-type solid electrolyte structure are presented. First, the convergence test variation of the total energy cut-off and the k-points sampling are discussed in detail. The structural and thermodynamic properties i.e. lattice parameters and heats of formation are analysed and discussed for a better understanding of the structure. Moreover, the elastic properties i.e. elastic constants and elastic moduli are discussed to give an insight on the mechanical stability of the t-LLZO structure. Lastly, the energy band structure and density of state (DOS) are analysed and discussed to help determine to electronic stability of the structure. The results of the above-mentioned properties are discussed and analysed in detail, while comparing them with experimental and theoretical results from other studies.

3.2 Simulation procedure

The plane-wave based, spin-polarized first-principle DFT calculations were performed using the Vienna Ab-initio simulation package (VASP) [41]. In VASP, electron-ion interactions were described by projector-augmented wave (PAW) potentials [43]. The generalized gradient approximations (GGA) of Perdue-Burke-Ernzerhof (PBE) were used for the exchange-correlation functional. A 5x5x5 Monkhorst-pack grid for k-point sampling, and a cut-off energy of 500eV were used for calculating structural optimization of t-LLZO. In order to obtain accurate forces, the first Methfessel-Paxton method was invoked for Fermi-surface smearing with a width of 0.2 eV. The self-consistency convergence criterion for the energy was set to 10^{-5}eV, and geometry relaxation was considered converged when all forces were less than 0.01eV/Å using a conjugate-gradient algorithm.

3.3 Convergence test

Convergence test essentially implies optimizing the parameters of the structural unit cell. The optimized parameters are the plane wave-based cut-off energy in eV and the number of k-points to be sampled all over the Brillouin zone. Convergence test is a way to simplify a simulation and allow effective use of limited computing resources. To evaluate the accuracy and reliability of the simulation, it is important to find an appropriate initial input setup for simulation study. Density functional theory (DFT) obtains a test by using an iterative method, the self-consistent field (SCF) method. By calculating the energy difference, SCF determines ground state electron density by slightly changing the electron density. If the energy exceeds the global minimum and convergence is reached, the difference between the preceding step and the energy is less than a certain value (convergence threshold), the estimate is concluded.

3.3.1 Cut-off energy

The cut-off energy should be varied before any functional properties are calculated to ensure the accurate reliability of the total energy of the respective structure. In order to determine the appropriate cut-off energy value for the t-LLZO structure, structural energy optimization calculations were carried out with different cut-off energy within the GGA-PBE until a constant minimum energy within 0.01 eV was reached. The total energy variance as a function of the t-LLZO cut-off energy starting from 100 eV to 900 eV, respectively. A cut-off energy of 500 eV was chosen as the graph display a considered sufficient energy convergence. Then the same cut-off energy will be used for calculating the k-mesh value.

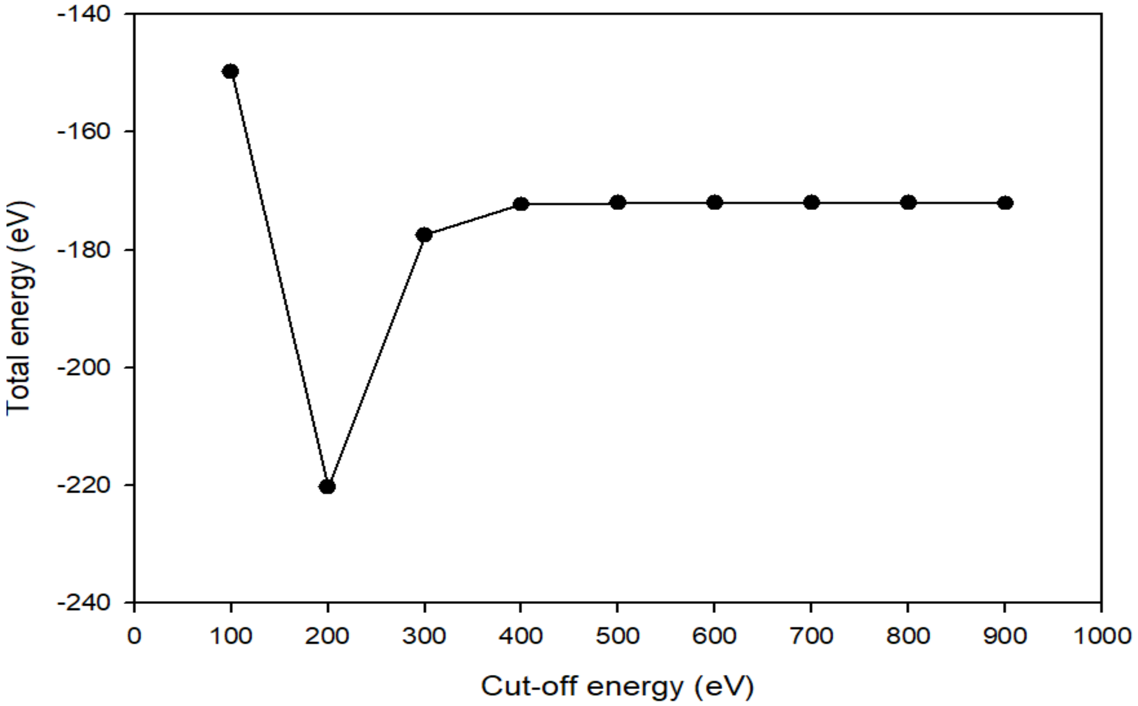

Figure 3.1: Variation of the total energy as a function of cut-off energy for t-LLZO compound.

3.3.2 K-Mesh points

K-points are sampling points in the material's first Brillouin zone i.e. the reciprocal-space zone closest to the centre (0, 0, 0) (usually referred to as the Gamma point). Having determined a suitable total energy cut-off, it is critical to determine the appropriate number of k-points to use in plane-wave pseudopotential calculations. The Monkhorst-Pack scheme was used to determine the appropriate set of k-points so that from the number of k-points used the greatest possible accuracy was achieved. The total energy calculation was performed at fixed cut-off energy of 500eV for t-LLZO while the number of k-points were varied from 1x1x1 to 9x9x9 until the total energy change is negligible and converged to within 1meV. A k-mesh point 5x5x5 was chosen for t-LLZO, as the graph in figure 3.2 display a considered sufficient energy convergence.

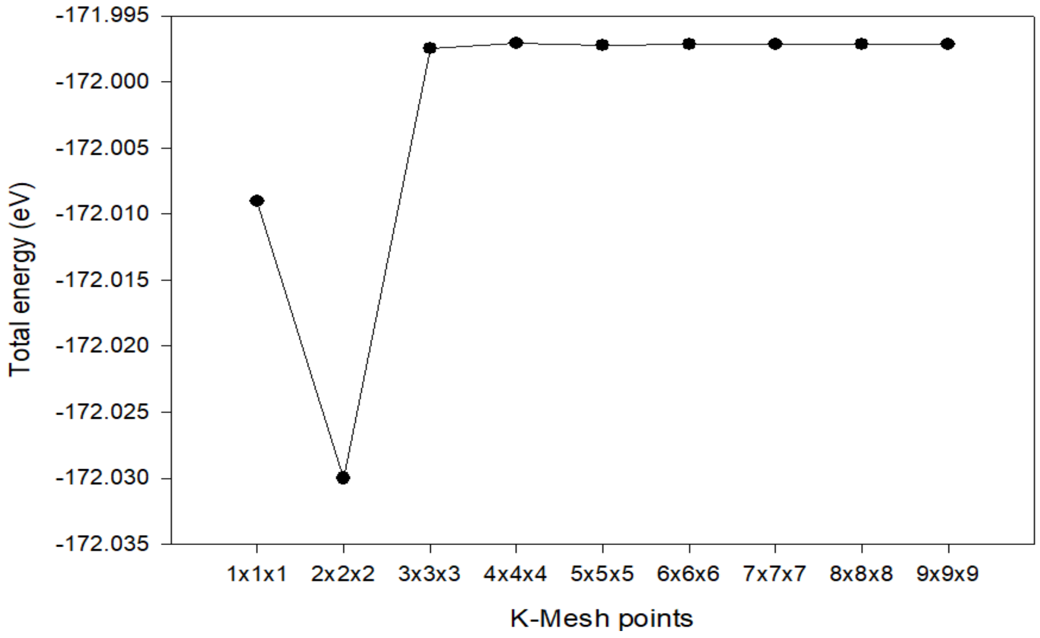

Figure 3.2: Variation of the total energy as a function of k-points for t-LLZO compound.

3.4 Structural Properties

The structural properties of material reflect the role of individual elements in its overall structure. In order to determine the structural properties, geometry optimization calculation was performed within the generalised gradient approximation using cut-off energy of 500eV and k-point sampling of 5x5x5. The optimization help relaxes the atoms in the structure, allowing the cell volume and lattice to reach the ground state energy. The optimized structure is then used for further calculation of the structural energy of formation. This section analyses and discusses the lattice parameters, cell volume and energy of formation of the t-LLZO crystal structure.

3.4.1 Crystal structure

The cut-off energy of 500 eV, and 5x5x5 Monkhorst-pack grid for t-LLZO, were used in optimizing the structure to obtain structural parameters, such as lattice constants (Å), energy of formation (kJ/mol) and equilibrium volume (Å). Table 3.1 lists the calculated and experimental lattice parameters, heats of formation, and cells volume of t-LLZO crystal structure. The optimized tetragonal (with space group $I4_1/acd$) LLZO crystal structure [6] is shown in figure 3.3 below. The lattice parameters of t-LLZO structure are a=b=13.12Å, and c=12.67Å, which are consistent with the experimental values of a=b=13.134Å, and c=12.663Å [14]. The heat of formation is calculated using GGA approximation. The heat of formation for t-LLZO is -6511.01kJ/mol, which indicate that the structure is thermodynamically stable. It is also noted that the calculated volumes for t-LLZO (2203m^3) is well adapted and compares well to the experimental value 2185m^3, which is within 0.824%.

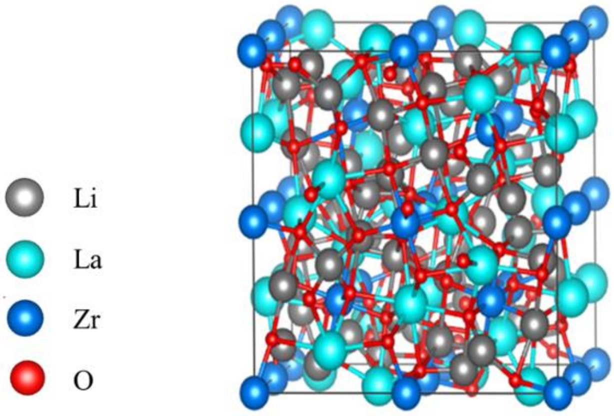

Figure 3.3: Crystal structure of garnet-type tetragonal $Li_7La_3Zr_2O_{12}$ (LLZO) with Li, La, Zr, and O ions shown in grey, turquoise, blue, and red, respectively.

Table 3.1: Calculated lattice constants (Å), energy of formation ΔH_f(kJ/mol), and volume V(Å) of t-LLZO compared with other experimental results.

	Tetragonal $Li_7La_3Zr_2O_{12}$	
	This work	Experimental
Lattice constant (Å)	a=b=13.1229 c=12.6648	a=b=13.1340 c=12.663
Energy of formation ΔH_f(kJ/mol)	-6511.01	-
Volume V(Å)	2203	2185 [14]

3.5 Elastic properties

In order to determine the elastic properties of the crystal structure, first-principle DFT elastic properties calculations i.e. elastic constants and elastic moduli were performed. The elastic constants are analysed and discussed in detail in order to determine the mechanical stability of the material. The shear modulus (G), bulk modulus (B), Young's modulus (E) and Pugh's ratio (v) are presented and discussed in this section for better understanding of the structure's strength against deformation.

3.5.1 Elastic constants

Elastic constants are important for several practical applications linked to the mechanical property of solids, such as elastic stress, internal strain, and fracture toughness. The response of a crystal to external forces is determined by its elastic constants. They play an important role in determining the strength of the material. A density functional theory approach was used to determine t-LLZO elastic constants. Ab-initio calculations were performed within the GGA framework. The VASP code has been employed for the random atom configuration of the structure. The elastic constants (C_{11}, C_{12}, C_{13}, C_{16}, C_{33}, C_{44} and C_{66}) for the tetragonal structure, were calculated and are summarized in table 3.2 below. The elastic behaviour of the crystal structure are described by its matrix of second-order elastic constants:

$$C_{ij} = \frac{1}{V_0}\left(\frac{\partial^2 E}{\partial \varepsilon_i \, \partial \varepsilon_j}\right) \qquad (3\text{-}1)$$

Table 3.2: Calculated elastic constants (C_{11}, C_{12}, C_{13}, C_{16}, C_{33}, C_{44} and C_{66}) of t-LLZO compound.

	Tetragonal $Li_7La_3Zr_2O_{12}$	
	t-LLZO	Experimental
C_{11}	177.69	169.80
C_{12}	85.46	63.90
C_{13}	80.42	-
C_{16}	1.91	-
C_{33}	205.05	-
C_{44}	76.51	69.80
C_{66}	71.27	-

Experimental values from Refs. [67]

The elastic constants are calculated to predict the mechanical stability of the materials. The elastic coefficients describe the crystal's mechanical and dynamic behaviour and show how it deforms under pressure and then returns to its initial shape. Table 3.2 shows elastic coefficients (C_{11}, C_{12}, C_{13}, C_{16}, C_{33}, C_{44} and C_{66}) values calculated using GGA approximation. It is observed that the elastic constants are all positive, which indicate a good mechanical stability. Thus, the elastic stability of t-LLZO is concluded using the results obtained from Table 3.2 and combining them with the formula (equation 3-2) below [68]:

$$C_{11} + 2C_{12} > 0$$

$C_{11} - C_{12} > 0$ (3-2)

$C_{11} > 0, C_{44} > 0$ And $C_{11}>0$; $C_{11}C_{16}> C^2_{12}$; $C_{44}>0$; $C_{55}>0$; $C_{66}>0$

3.5.2 Elastic modulus

The elastic modulus of a material indicates how resistant it is to being deformed elastically when under stress. From the calculated elastic constants, the elastic moduli have been determined using Hills. The modulus are used to describe the elastic behaviour of materials. The calculated shear modulus (G), bulk modulus (B) and Young's modulus (E) are presented in table 3.3 below. Furthermore, the poison's ratio (v) and the Pugh's ratio (B/G) were calculated.

Table 3.3: Calculated Bulk (B), Shear (G) and Young modulus (E), and Pugh ratio (B/G) modulus of t-LLZO using GGA approximation.

	Tetragonal $Li_7La_3Zr_2O_{12}$		
	This work	Experimental [67]	Other [64]
Bulk modulus B (GPa)	112.23	99.20	111.42
Shear modulus G (GPa)	64.84	62.50	64.98
Young modulus E (GPa)	163.51	154.90	163.11
Pugh ratio B/G	1.73	1.59	1.71
Poisson's ratio v	0.258	0.24	0.26

According to the Hill approximations, the bulk modulus (B) and Shear modulus (G) can be obtained from the values of elastic coefficients (C_{11}, C_{12}, C_{13}, C_{16}, C_{33}, C_{44} and C_{66}). It is also possible to calculate the values of Young's modulus (E) and Poison ratio using the following formula: [64]

$$B = \frac{C_{11} + 2C_{12}}{3} \quad (3\text{-}3)$$

$$G = \frac{\left[\frac{C_{11} - C_{12} + 3C_{44}}{5}\right] + \left[\frac{5C_{44}\,(C_{11} - C_{12})}{[4C_{44} + 3(C_{11} - C_{12})]}\right]}{2} \quad (3\text{-}4)$$

$$E = \frac{9BG}{3B+G} \quad (3\text{-}5)$$

$$v = \frac{3B-E}{6B} \quad (3\text{-}6)$$

From table 3.3, several important points are noted. The calculated values for G, B, E, B/G and v are 112.23 GPa, 64.84 GPa, 163.51 Gpa, 1.73 and 0.258, respectively. These values are in good agreement with the DFT (0K) data showing a percentage difference of ~3%. The bulk modulus is a measure to evaluate the crystal's strength and hardness, which describes the crystal's strength against brittleness, whenever the Bulk modulus is higher, and the crystal has greater strength. Comparing the calculated values from Table 3.3 and the values obtained from other works (Table 3.3), t-LLZO has the highest B values, while experimental has the lowest values. The reason for the small difference between them is due to the difference between the method used and approximation. The shear modulus (G) demonstrates the strength of t-LLZO material to supress lithium dendrite formation, which in this case it is stiff enough. The Young's modulus (E) is a measure of a material's stiffness. When E is larger, the material is considered stiffer. From the table 3.3 above, it is clear that the Young's modulus of t-LZO is much greater than that of the experimental since it has the highest value of E. This implies that t-LLZO structure is mechanically stronger. Pugh introduced the ratio of bulk to shear modulus (B/G), which is used to present an evaluation of the softness or hardness of the material [69].

$\frac{B}{G} > 1.75$ implies that the material is ductile

$\frac{B}{G} < 1.75$ implies that the material is brittle

The calculated Pugh ratio B/G for t-LLZO is 1.73 which indicates that the material is intrinsically brittle, showing an agreement with the data from other works, and the 0.258 Poisson’s ratio means that the material is predominantly ionic, hence it can be used in solid state Li batteries.

3.6 Electronic properties

The electronic properties of a material are a set of parameters and representations that describe the state and behaviour of electrons within it. In order to determine the electronic properties of t-LLZO, the energy band structure and density of state (DOS) of t-LLZO were performed using first-principle DFT calculations within generalized gradient approximation (GGA). The calculated properties are significant because they illustrate how the LZO structure behaves under normal conditions. In this section, the calculated band structure and density of state plots are analysed and discussed in detail.

3.6.1. Band structure curves

In the curves of the band structures, the energy function is plotted in the first brillouin zone versus the energy (eV). From this diagram, some important information on the crystal-electronic nature of being metal or non-metal, the energy gap gage can be obtained if it exists, the type of energy gap being direct or indirect, the effective mass, the velocity and mobility of the carrier and so on. In figure 3.4 is the t-LLZO band structure diagrams using GGA. The distance between the states at the maximum valence band (VBM) and the minimum conductive band (CBM) is determined by the electronic band gap. As a result, the below plotted band structure curves show that t-LLZO is an insulator with a large band gaps of 4.33eV by GGA approximation located at the gamma-point of the brillouin zone. The band gap is in good agreement with the experimental data from other studies which indicate that a wide electrochemical window is an intrinsic property of LLZO, facilitating its use in next-generation batteries.

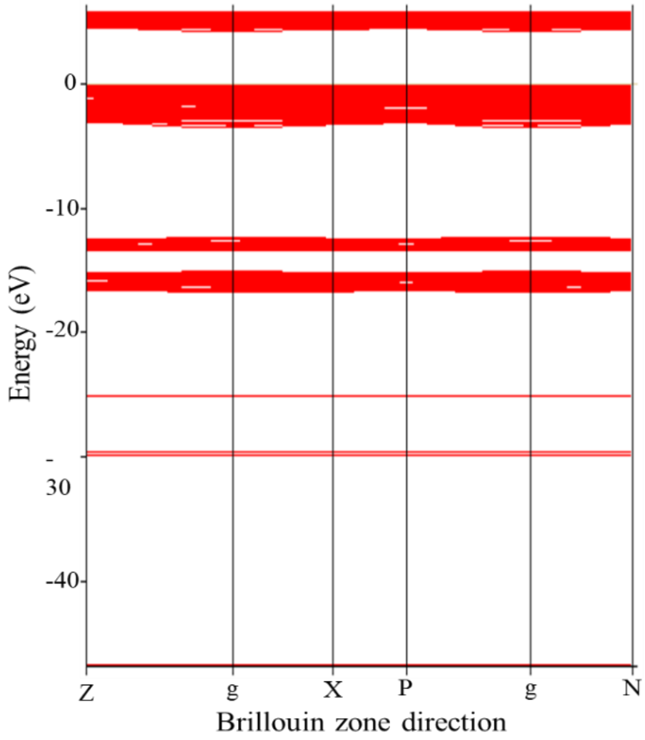

Figure 3.4: Band structures for t-LLZO solid electrolyte at equilibrium pressure.

3.6.2 Density of state

Density of states describes the probability of electron distribution in the energy spectrum. The total density of state calculations using GGA approximations for $Li_7La_3Zr_2O_{12}$ in tetragonal solid electrolyte phase at equilibrium pressure is shown in Figure 3.5, in which Fermi energy is chosen as a zero point of reference. The upper plot shows the total density of states (TDOS), and the lower plots show partial density of states (PDOS) for Li, La, Zr, and O. The TDOS indicates the total contributions of all atoms in the structure, whereas the PDOS indicates the contributions of individual atoms. By comparison between figure 3.4 and figure 3.5, a significant adaptation has been shown between density of states and band structure calculations. It is clear that the total density of states can be divided into three different regions; the region of the lower valence band (LVB) in the range of −18.5 to −12 eV, which is due to orbitals of La-p and O-s, the region of the upper valence band (UVB) in the range of −4 to 0 eV, which is due to orbitals of Li-p, Zr-f and O–p, can be shown to be the result of the hybridization of the valence band, the last region is related to the conduction band (CB) and the edge of the conduction band, as shown in figure 3.5, is related to the atoms Li and La of the orbitals p and f, respectively. The t-LLZO further confirms the insulator behaviour as shown by band structure, since there is a large band gap formed at the p orbital of the Li atom, and the energy of the band gap is similar to that given by the band structure (4.33eV).

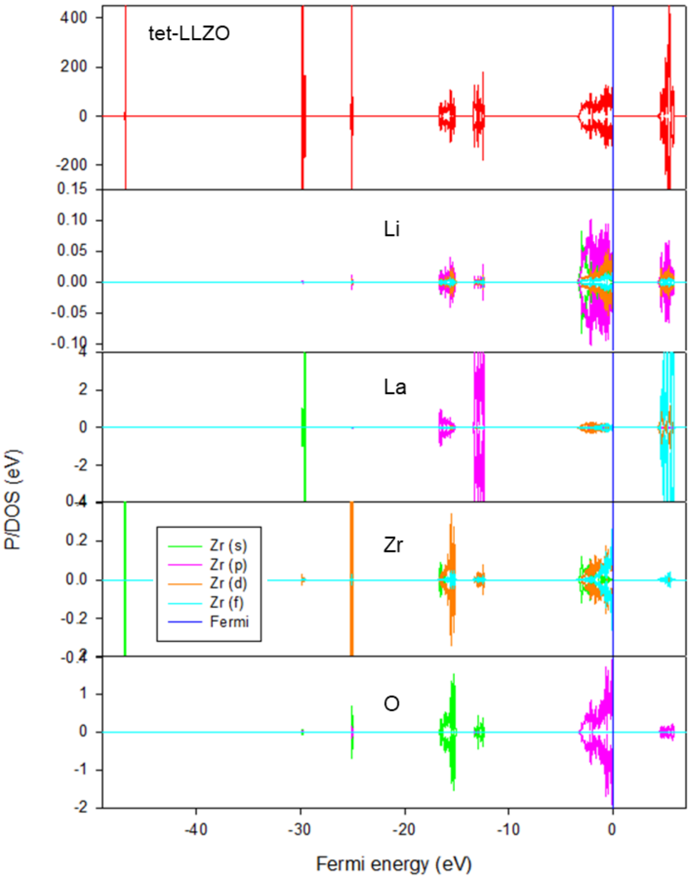

Figure 3.5: Density of states of the t-LLZO solid-state electrolyte.

CHAPTER 4: First-Principle Cluster Expansion Study of Ta-doped Tetragonal $Li_7La_3Zr_2O_{12}$ (t-LLZO) Oxide-Garnet Solid-State Electrolyte.

4.1. Introduction

Predicting the phase stability of solid-state electrolytes is crucial for materials design and development. In this chapter, the calculation results of DFT combined with cluster expansion and Monte Carlo calculations performed on the t-LLZO are presented. Oxide $Li_7La_3Zr_2O_{12}$ (LLZO) solid electrolyte has become increasingly important in solid-state lithium-ion batteries. Extensive research has been done in both experimental investigations and theoretical simulations aiming to improve its performance. These include developing different methods for the study of LLZO, using different temperatures to stabilize the crystal structure, and adopting different methods of cation doping to achieve stable LLZO with high ionic conductivity. Nonetheless, a more insightful study is expected in order to improve LLZO with a higher ionic conductivity at room temperature with good phase stability and further improve structural, mechanical, and electronic stability, and supervalent cation doping is considered to be a feasible and promising strategy.

The binary ground-state diagram obtained from cluster expansion calculations is discussed and analysed in detail to understand Ta-doped LLZO phase stability and to generate new possible phases. Monte Carlo temperature profiles are analysed to gain an understanding of the behaviour of the Ta-doped phase in a canonical ensemble at different temperatures. Further density functional theory calculation results on the most generated stable $Li_5La_3Zr_{2-x}Ta_xO_{12}$ structures are discussed and analysed in detail to determine the structural, mechanical, and electronic properties of the structure for its applications as an active solid-state electrolyte. The results of the above-mentioned properties are discussed and analysed in detail, while comparing them with results of pure t-LLZO from this studies to check if there is an improvement in terms of the stability of the structures.

As an appropriate computational method, cluster expansion is a power series expansion of the partition function which was proposed by Mayer in 1941. Cluster expansion is often applied as a pipeline that combines first-principle calculations and Monte Carlo simulation which aims at estimating the properties of the material. First-principles calculations give accurate energy calculations, however, the implementations are limited to a few hundred atoms per unit cell, and so the DFT calculations are very slow, highly computationally demanding since they do not scale well with system size. For the following reasons, the cluster expansion (CE) method is the most suitable energy model: the energy of a large system with thousands of or more atoms can be calculated very fast; accurate and transferable CE coefficients can be obtained by fitting to energies of DFT calculations for a selected set of small structures, most importantly generate multi-component structures within a random mixing. With the CE method for the energy model, it is very typical to use lattice Monte Carlo (MC) simulation to investigate the atomic structure of oxide LLZO solid electrolytes at a nano-scale.

The Monte Carlo calculations based on the converged cluster expansion are conducted in order to incorporate temperature effects on the system. Monte Carlo (MC) is a stochastic method commonly used in thermodynamic statistics. It is primarily used to estimate integrals and calculate mean values, as well as to evaluate phase stability as a function of temperature. The MC temperature profiles at concentrations that correspond to the concentrations of the most stable generated CE structures give a clearer view of the temperature effect on the system for better analysis and discussion. With the most stable generated $Li_5La_3Zr_{2-x}Ta_xO_{12}$ structures, further DFT calculations such as; lattice constants, energy of formation, volume, elastic constants, elastic modulus, and band structures are performed to evaluate their stability in terms of structure, elasticity and electronic behaviour.

4.2. Simulation procedure

In this study, an accurate and efficient energy model based on the cluster expansion method is developed for $Li_5La_3Zr_{2-x}Ta_xO_{12}$. The atomic structures of $Li_5La_3Zr_{2-x}Ta_xO_{12}$ are then investigated by Monte Carlo simulation in combination with the cluster expansion method. To search for the ground state clusters, the universal cluster expansion (UNCLE) code uses a genetic algorithm (GA) to identify an optimum set of clusters with their corresponding interaction parameters obtained from the energies of structures contained in a training set. The energies of the structures contained in the training set are calculated by using a DFT method. The structures are selected according to the CE flowchart settings (discussed in chapter 2). The effective structures are iteratively added to the training set, and convergence is achieved when no new ground-state structures are found by CE.

From the converged CE, a set of effective cluster interactions is extracted and used in large-scale Monte Carlo simulation to explore order-disorder phenomena and phase separation process as a function of temperature under canonical ensemble. The MC temperature profiles are performed at various temperatures and concentrations. The concentrations are set in a way that corresponds to the concentrations of the most stable CE-generated $Li_5La_3Zr_{2-x}Ta_xO_{12}$

structures from a binary ground-state diagram for better understanding and interpretation of the results. The crystal structure optimization, elastic and electronic calculations of the most stable CE generated structures are further performed using DFT.

The geometry optimization of t-LLZO is discussed in chapter 3. From the optimized t-LLZO, the MedeA-Universal Cluster Expansion (UNCLE) [57] package was used, which allows the set up to construct and automatically converge the CE for t-LLZO to generate the unique clusters within the random mixing. A set of effective cluster interactions from an optimized cluster expansion calculation is extracted and used in large-scale Monte Carlo simulations. The MC simulations in the UNCLE package uses a 5x5x5 supercell with 11000 atoms under a canonical ensemble at different temperatures and concentration. The structure optimization and electronic structure calculations for the most stable generated CE $Li_5La_3Zr_{2-x}Ta_xO_{12}$ structures are performed using VASP and its efficient implementation of density functional theory methods, which is fully integrated in the MedeA software environment MedeA [70]. The electron-ion interactions were solved using the projector-augmented wave (PAW) potentials [43]. The exchange-correlation functionals were accounted for by parameterizations of the generalized-gradient approximation (GGA) of Perdue-Burke-Ernzerhof (PBE). A 5x5x1 Monkhorst-pack grid for k-point sampling, and a cut-off energy of 500eV were used for calculating structural optimization of $Li_5La_3Zr_{2-x}Ta_xO_{12}$ structures. In order to obtain accurate forces, the first Methfessel-Paxton method was invoked for Fermi-surface smearing with a width of 0.2 eV. The self-consistency convergence criterion for the energy was set to 10^{-5}eV, and geometry relaxation was considered converged when all forces were less than 0.01eV/Å using a conjugate-gradient algorithm.

4.4. Results and discussions

In this section, the binary ground-state CE diagram and Monte Carlo temperature profile results generated from cluster expansion and Monte Carlo simulation are discussed in details for a better understanding of the generated structures and their behaviour under the effect of temperature. The cross validation score (CVS) and the number of iterations are discussed in detail for a clearer analysis of the ground-state search. Further detailed analysis on the most stable generated is attained through the discussion of the structural, mechanical and electronic properties of the structures. For a better analysis of the structural properties of the most stable Ta-doped structures, the lattice parameters, heats of formation and volume calculations are discussed in detail. The elastic constants and elastic modulus of the most stable Ta-doped structures are discussed in detail to give better understanding of the mechanical properties of the structures. Lastly, the band structures of the most stable Ta-doped structures are discussed in detail for a better analysis of the electronic properties of the generated CE structures.

4.4.1. Binary ground-state diagram

The ground-state search of new structures was conducted using 1-unit cell, which made it easier for the CE ground-state search calculations since the arrangement of atoms in the oxide garnet LLZO crystal structure are complex. The structures were generated following the automatic ground-state search procedure illustrated in figure 2.3 (discussed in chapter 2). The effective cluster interactions were fitted by means of a GA. The fitting scheme calculated for a maximum of 23 iterations, adding a maximum of 9 new structures in each iteration, and starting from an initial training set of 20 structures. The iterations continued until there were no new structures predicted by the CE. Table 4.1 below shows the number of iterations used to converge the ground state search, the number of structures in the ground state, the number of new structures in the ground state, the cross validation score to predict the accuracy of DFT energy calculations, the standard deviation to predict whether there will be errors in the MC calculations or not, and lastly the list of generated new structures per iteration. To conduct the search, the parent structures $Li_5La_3Zr_2O_{12}$ and $Li_5La_3Ta_2O_{12}$ were used, which are the 2 new structures generated across the first iteration 0. The generated 20 new structures across the second iteration 0 are the initial structures in the training set randomly identified by the UNCLE code using a genetic algorithm. Optimum set of new structures are identified with their corresponding interaction parameters from the energies of the structures contained in the training set, that is the structures generated from iteration 1 up until iteration 22. The last iteration is used to predict whether the CE ground-state search has converged or not. In order for the search to converge, the last iteration must generate 0 new structures. From table 4.1 below, it is observed that at iteration 23 there are 0 new structures which implies that the CE ground-state search has converged. Moreover, this implies that the DFT energy evaluation within CE was achieved. The cross-validation process is a statistical procedure used to assess the structures reliability. Most commonly, it is used for prediction and estimating how accurate a predicted structure will be in practice. It is more indicative of the generalization ability of the structures because it has not been used during training. From table 4.1 below, the cross validation score (CVs) for all the generated new structures is less than 5meV per active atom position, which implies accuracy in generation of new structures during CE fitting. The standard deviation of the energy predictions was not evaluated since all the generated structures have a CVs below 5meV, which implies that the calculations were accurate and the new generated structures will function practically.

Table 4.1: List of generated new structures. Table re-plotted from a MedeA interface job.out file.

Iteration	No. of struc.	No. of new struc.	CVS [meV/pos.]	% struc. with SD below 5 meV	New structures
0	0	2	-	-	ce1 ce2
0	0	20	-	-	ce1 ce4 ce13 ce11..
1	20	9	0.45	-	ce22 ce21 ce19 ...
2	20	9	0.45	-	ce22 ce21 ce19 ...
3	20	9	0.45	-	ce22 ce21 ce19 ...
4	20	9	0.45	-	ce22 ce21 ce19 ...
5	20	9	0.45	-	ce22 ce21 ce19 ...
6	20	9	0.45	-	ce22 ce21 ce19 ...
7	20	9	0.45	-	ce22 ce21 ce19 ...
8	20	9	0.45	-	ce22 ce21 ce19 ...
9	20	9	0.45	-	ce22 ce21 ce19 ...
10	20	9	0.45	-	ce22 ce21 ce19 ...
11	20	9	0.45	-	ce22 ce21 ce19 ...
12	20	9	0.2	-	ce22 ce21 ce19 ...
13	21	9	0.26	-	ce22 ce21 ce19 ...
14	21	9	0.33	-	ce22 ce21 ce19 ...
15	21	9	0.25	-	ce22 ce21 ce19 ...
16	21	9	0.2	-	ce22 ce21 ce19 ...
17	21	9	0.33	-	ce22 ce21 ce19 ...
18	21	9	0.25	-	ce22 ce21 ce19 ...
19	21	9	0.34	-	ce22 ce21 ce19 ...
20	21	9	0.26	-	ce22 ce21 ce19 ...
21	21	9	0.26	-	ce22 ce21 ce19 ...
22	21	9	0.25	-	ce22 ce21 ce19 ...
23	21	0	0.34	-	

The entropy of formation as a function of Ta concentration binary ground-state diagram obtained from the cluster expansion calculations is shown in figure 4.1 below. The binary ground state diagram summarises the generation of new structures, and prediction of formation of the structures considered by the CE. From figure 4.1 below, the green crosses show the CE predicted enthalpies of formation of the structures in training set. The green squares show the DFT enthalpies of formation of the structures in the training set. The grey crosses predict formation of all the other structures considered by the CE. The binary ground state diagram generated 28 new structures with different concentration and symmetries. The pure phases $Li_5La_3Zr_2O_{12}$ and $Li_5La_3Ta_2O_{12}$, which are the parent structures, are located on the solid-black line lying on X=0 and X=1, respectively. The red solid line is the ground-state line, with structures on it considered being the most stable. The structures with positive enthalpy of formation, are considered not stable by the CE since the structures are generated through non-spontaneous process, meaning the structures could be stable at higher or lower temperatures. Also the structures depend on external force for natural occurrence. In figure 4.1 below, it is observed that the ground-state line (red solid line) is formed in the negative site of the enthalpy of formation whereby all the generated structures have negative enthalpy of formation, which implies that the structures are thermodynamically stable. However, the structures obtained on the solid-red line are considered the most stable which are $Li_5La_3ZrTaO_{12}$ ($P\bar{1}$), $Li_5La_3Zr_{0.5}Ta_{1.5}O_{12}$ (C2/c), $Li_5La_3Zr_{1.5}Ta_{0.5}O_{12}$ ($P\bar{1}$), $Li_5La_3Zr_{1.75}Ta_{0.25}O_{12}$ ($P\bar{1}$), and $Li_5La_3Zr_{0.25}Ta_{1.75}O_{12}$ ($P\bar{1}$). The structures have different concentrations of zirconium and tantalum: $Li_5La_3ZrTaO_{12}$ ($P\bar{1}$) has 50% Zr concentration and 50% Ta concentration, $Li_5La_3Zr_{0.5}Ta_{1.5}O_{12}$ (C2/c) has 25% Zr concentration and 75% Ta concentration, $Li_5La_3Zr_{1.5}Ta_{0.5}O_{12}$ ($P\bar{1}$) has 75% Zr concentration and 25% Ta concentration, $Li_5La_3Zr_{1.75}Ta_{0.25}O_{12}$ ($P\bar{1}$) has 87.5% Zr concentration and 12.5% Ta concentration, lastly $Li_5La_3Zr_{0.25}Ta_{1.75}O_{12}$ ($P\bar{1}$) has 12.5% Zr concentration and 87.5% Ta concentration.

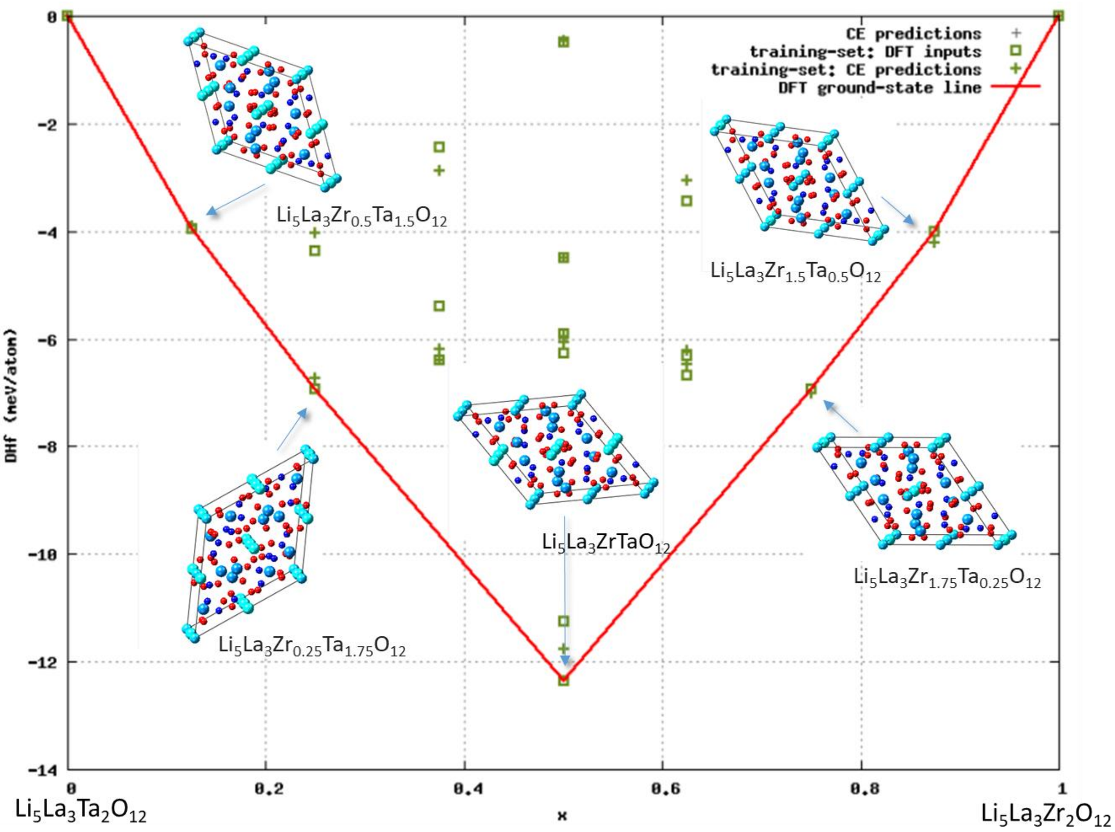

Figure 4.1: Binary ground-state diagram of $Li_5La_3Zr_{2-x}Ta_xO_{12}$ oxide solid electrolyte.

4.4.2. Monte Carlo temperature profile

Monte Carlo is used to determine thermodynamic averages, thermodynamic potentials (from the averages), and study phase transition processes as a function of temperature. From the optimized cluster expansion, a set of effective cluster interactions were extracted and used in large-scale Monte Carlo simulations to explore the states of the system stochastically with probabilities that match those expected physically. In order to evaluate the phase stability of the $Li_5La_3Zr_{2-x}Ta_xO_{12}$ compounds, Monte Carlo simulation was performed from the converged CE. The simulation was carried out under canonical ensemble for a better understanding of the phase separation process as a function of temperature. A 5x5x5 super cell containing 11000 atoms was used, whereby the minimum average number of steps was 300000 with initial temperature of 200K and a final temperature set to 3000K. The energy convergence was set to 0.0001 Å. The concentration was set based on the concentration of the most stable generated structures in order to analyse the behaviour of the structures at a specified temperature.

Figure 4.2 (a-c) below show Monte Carlo temperature profile at different concentrations of Zr and Ta. The temperature profile shown in figure 4.2 (a-c) below at concentrations (a) $Zr_{0.5}Ta_{0.5}$, (b) $Zr_{0.25}Ta_{0.75}$ and (c) $Zr_{0.125}Ta_{0.875}$, correspond to the stable structures $Li_5La_3ZrTaO_{12}$ ($P\bar{1}$),

$Li_5La_3Zr_{0.5}Ta_{1.5}O_{12}$ (C2/c), and $Li_5La_3Zr_{0.25}Ta_{1.75}O_{12}$ ($P\bar{1}$) from CE, respectively. Figure 4.2 at concentration $Zr_{0.5}Ta_{0.5}$ shows that the atoms mix very well at ~800K, also the system shows a very small energy difference of 0.9eV/atom. Zirconium and tantalum tend to mix very well since both metals have similar properties in a sense that they have high melting point which indicate strong intermolecular interactions of atoms, and both are resistant to correction. The temperature profile at concentrations $Zr_{0.25}Ta_{0.75}$ mix well at ~1000K with energy difference of 0.61eV/atom. The temperature profile at concentrations $Zr_{0.125}Ta_{0.875}$mix well at ~800K with energy difference of 0.45eV/atom. At concentrations $Zr_{0.5}Ta_{0.5}$ and $Zr_{0.125}Ta_{0.875}$ the critical temperature is the same (~800K), this is because the corresponding structures $Li_5La_3ZrTaO_{12}$ ($P\bar{1}$) and $Li_5La_3Zr_{0.25}Ta_{1.75}O_{12}$ ($P\bar{1}$) have the same symmetry. It is observed that the energy difference decrease as the Ta concentration increase. This is because tantalum has higher melting point compared to zirconium, meaning it can withstand high temperature. Hence, the generated structures with high concentration of tantalum are expected to operate well at high temperature.

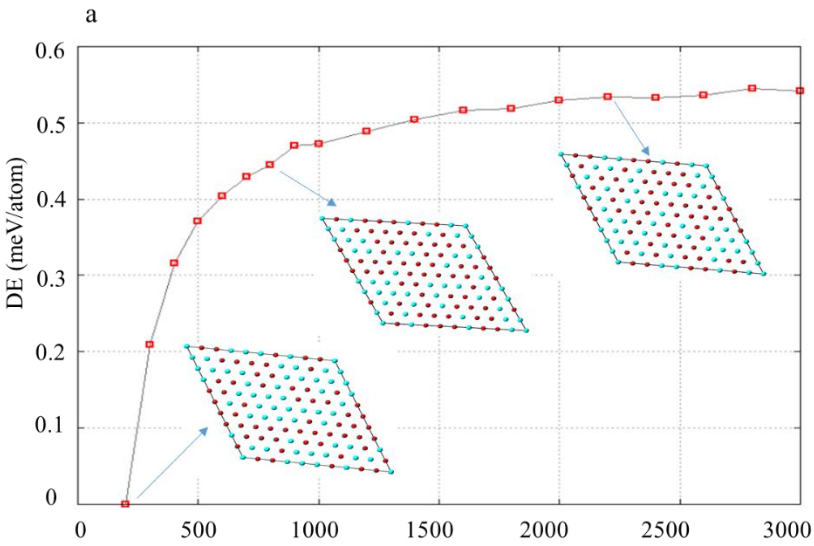

Figure 4.2: Monte Carlo temperature profile of $Li_5La_3Zr_{2-x}Ta_xO_{12}$ at different concentrations (a) $Li_5La_3ZrTaO_{12}$ (P1)

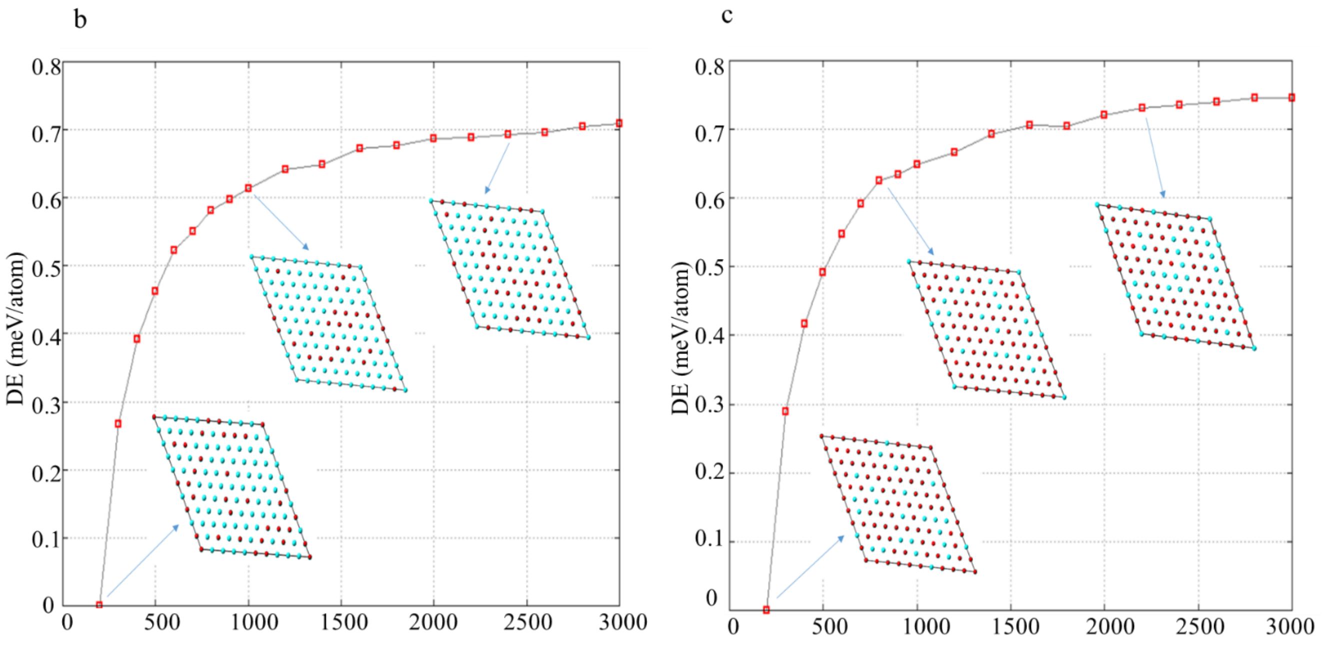

Figure 4.2: Monte Carlo temperature profile of $Li_5La_3Zr_{2-x}Ta_xO_{12}$ at different concentrations (b) $Li_5La_3Zr_{0.5}Ta_{1.5}O_{12}$ (C2/c), and (c) $Li_5La_3Zr_{1.5}Ta_{0.5}O_{12}$ (C2/c)

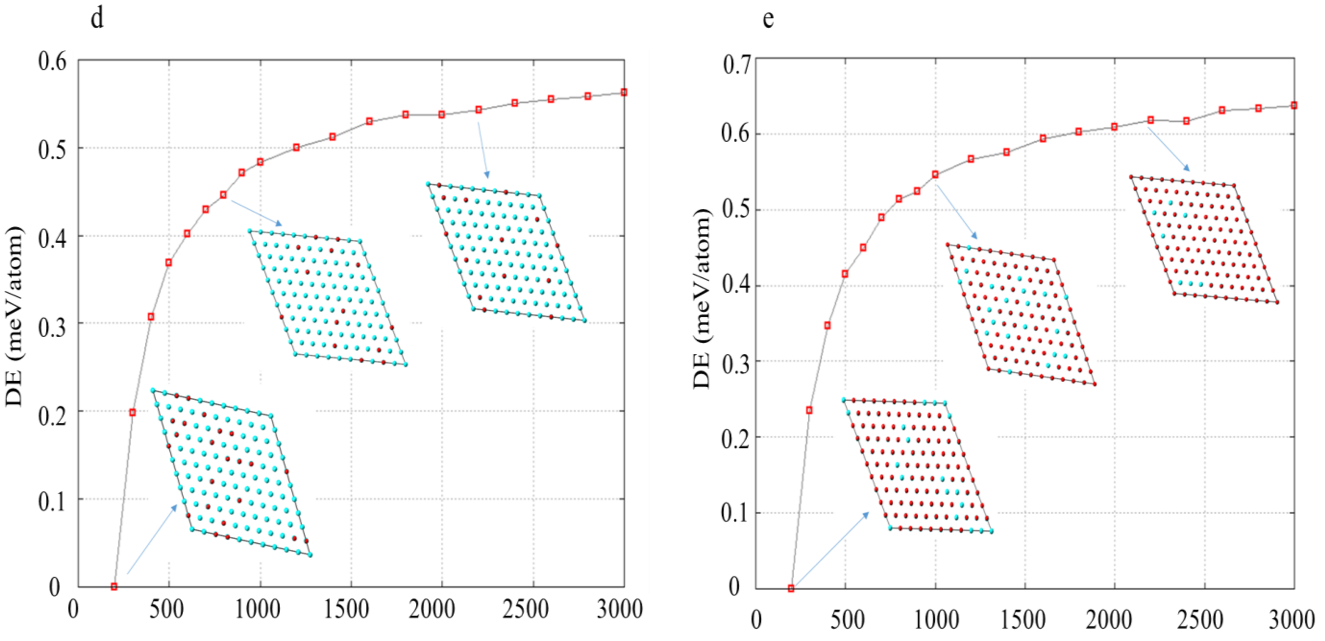

Figure 4.2: Monte Carlo temperature profile of $Li_5La_3Zr_{2-x}Ta_xO_{12}$ at different concentrations (d) $Li_5La_3Zr_{0.25}Ta_{1.75}O_{12}$ (P1), and (e) $Li_5La_3Zr_{1.75}Ta_{0.25}O_{12}$ (P1)

4.4.3 The cluster expansion stable structures

The most stable structures generated from the binary ground-state CE diagram are further evaluated for better comparison with the pure t-LLZO structure. Figure 4.3 (a-c) shows the most stable CE generated structures which were visualised using VESTA software. The structures have different symmetries and concentrations, this is because for a partial fraction of Zr^{4+} atoms to be doped by Ta^{5+} atoms in the 16c octahedral Zr site of t-LLZO the search algorithm proceed as follows: First, a single doping of Ta to Zr is made for each symmetrically independent Zr site, hereby generating a set of new structures. The structures resulting from the operation are grouped by their new symmetries. Next, for each Zr of the new set of structures, a second substitution is performed on each symmetrically independent Zr site; again the resulting structures are regrouped according to symmetry, and the process is repeated up to the desired number of doping. Different symmetries were generated, however, with unbalanced charge, thus the Li concentration had to be adjusted in order to maintain charge neutrality. Li atoms are either removed (as vacancies) from the highest energy sites or added (as interstitials) to the lowest energy sites, according to an electrostatic energy criterion. In this case, the Li vacancies were created in order to maintain charge neutrality of the new possible structures. From figure 4.3 (a-c) it is observed that figure 4.3 (a) has different arrangement of atoms compared to figure 4.3 (b) and (c), however all the structures have 88 atoms with different Wyckoff position (see table 4.2-4.4). It is observed that Zr and Ta atoms in table 4.2 and table 4.4 have the same Wyckoff equation of (0, 0, 0) with the Wyckoff position 1a and 1b, respectively. This is because $Li_5La_3ZrTaO_{12}$ and $Li_5La_3Zr_{0.25}Ta_{1.75}O_{12}$ have the same space group of P1. For better understanding of these promising generated CE structures the structural, elastic and electronic properties calculations were performed in order to determine the stability of these structures as active solid-state electrolytes.

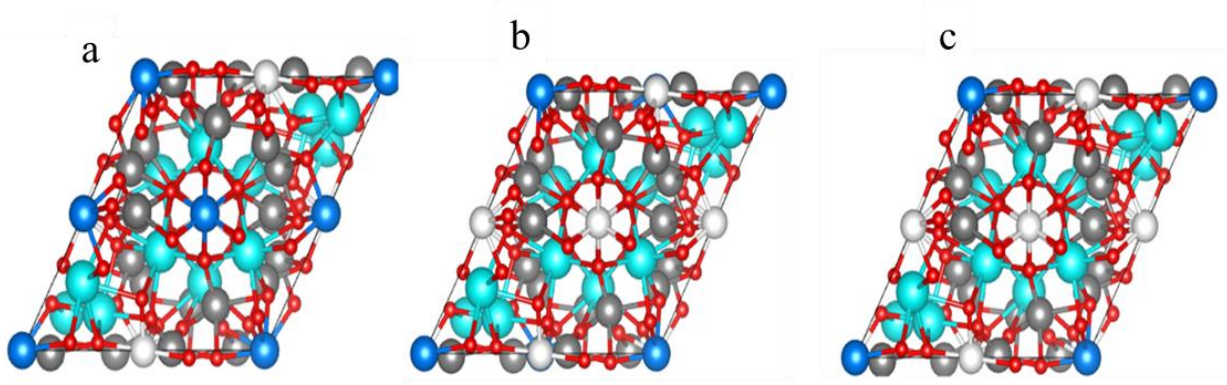

Figure 4.3: The most stable CE generated Ta-doped $Li_5La_3Zr_{2-x}Ta_xO_{12}$ structures (a) $Li_5La_3ZrTaO_{12}$ (P1), (b) $Li_5La_3Zr_{0.5}Ta_{1.5}O_{12}$ (C2/c) and (c) $Li_5La_3Zr_{0.25}Ta_{1.75}O_{12}$ (P1).

Table 4.2: Fractional coordinates, Wyckoff positions, and Wyckoff equations of sites occupied by constituent atoms of $Li_5La_3ZrTaO_{12}$ (P1).

Atoms	Wyckoff Positions	Wyckoff equation	x	y	z
Li (1)	32g	x, y, z	0.917	0.586	0.694
Li (2)	16f	x, x + 1/4, 1/8	0.676	0.929	0.625
Li (3)	8a	0, 1/4, 3/8	0.5	0.75	0.875
La (1)	16e	x, 0, 1/4	0.628	0.5	0.75
La (2)	8b	0, 1/4, 1/8	0.5	0 .75	0.625
Zr	1a	0, 0, 0	0	0	0
Ta	1b	0, 0, 1/2	0	0	0.5
O	32g	x, y, z	0.701	0.819	0.419

Table 4.3: Fractional coordinates, Wyckoff positions, and Wyckoff equations of sites occupied by constituent atoms of $Li_5La_3Zr_{0.5}Ta_{1.5}O_{12}$ (C2/c).

Atoms	Wyckoff Positions	Wyckoff equation	x	y	z
Li (1)	8f	x, y, z	0.331	0.163	0.887
Li (2)	8f	x, y, z	0.331	0.336	0.892
Li (3)	8f	x, y, z	0.586	0.419	0.892
La (1)	4e	0, y, 1/4	0	0.372	0.25
La (2)	8f	x, y, z	0.622	0 .25	0.122
Zr	4d	1/4, 1/4, 1/2	0.25	0.25	0.5
Ta	4a	0, 0, 0	0	0	0

O	8f	x, y, z	0.647	0.054	0.181

Table 4.4: Fractional coordinates, Wyckoff positions, and Wyckoff equations of sites occupied by constituent atoms of $Li_5La_3Zr_{0.25}Ta_{1.75}O_{12}$ (P1).

Atoms	Wyckoff Positions	Wyckoff equation	x	y	z
Li (1)	2i	x, y, z	0.495	0.225	0.108
Li (2)	2i	x, y, z	0.75	0.625	0.125
Li (3)	2i	x, y, z	0.25	0.875	0.375
La (1)	2i	x, y, z	0.628	0.5	0.75
La (2)	2i	x, y, z	0.5	0 .75	0.625
Zr	1a	0, 0, 0	0	0	0
Ta	1b	0, 0, 1/2	0	0	0.5
O	2i	x, y, z	0.701	0.819	0.089

4.4.4. Structural Properties of Ta-doped LLZO

The structural properties of a material reflect the role of individual elements in the overall structure. It is important to analyse the structural properties of the generated CE structures for a better understanding of the effect of the doped tantalum to the t-LLZO in terms of lattice parameters, energy of formation and volume. The lattice parameters are the quantities that specify a unit cell or the unit of the atomic arrangement's periodicity.

The lattice parameters (constants) namely a, b and c parameters which are the three-dimensional lengths of the unit cell. The amount of three-dimensional space enclosed by a closed surface is expressed as a scalar quantity called volume. A positive heat of formation indicates that more energy is used in breaking bonds than is released upon solute-solvent bond formation, then the overall process is endothermic. If the heat of formation is negative, more energy is released in making bonds than is used in breaking bonds, the overall process is exothermic. To evaluate the structural properties, geometry optimization calculations were performed within the generalised gradient approximation using the cut-off energy of 500eV and the k-point sampling of 5x5x1 for all the structures. The optimization help relaxes the atoms in the structure, allowing the cell volume and lattice to reach the ground state energy. The optimized structures are then used for further calculation of the structural energy of formation. This section analyses and discusses the lattice parameters, cell volume and energy of formation of the Ta-doped $Li_5La_3Zr_{2-x}Ta_xO_{12}$ structures.

Table 4.5: Calculated lattice constants (Å), energy of formation ΔH_f (kJ/mol), and volume V(Å) of Ta doped LLZO structures of space groups.

	$Li_5La_3ZrTaO_{12}$ (P1)	$Li_5La_3Zr_{0.5}Ta_{1.5}O_{12}$ (C2/c)	$Li_5La_3Zr_{0.25}Ta_{1.75}O_{12}$ (P1)
Lattice constant (Å)	a=b=c= 11.25Å	a=11.19Å b=c=11.23Å	a=b=11.16 Å c= 11.25Å
Energy of formation ΔH_f(kJ/mol)	-5959.82	-12068.84	-24290.23
Volume V(Å)	1091.80	1081.27	1077.49

The calculated lattice parameters, energy of formation and the cell volume for $Li_5La_3ZrTaO_{12}$ are shown in table 4.5 above. The parameters were calculated at an ambient pressure that correspond to the cell volume. From the table it is clear that the values of the calculated lattice parameters for all the generated structures are smaller than that of the pure tetragonal LLZO structure (discussed in chapter 3) which is expected since the ionic radius of Ta^{5+} (0.64 Å) is less than that of Zr^{4+} (0.72 Å). Moreover, the results show that the distance between Li-Li in doped Ta-LLZO is smaller than in pure t-LLZO which indicates that the smaller the difference between the dopant ionic radius and the critical dopant radius, the higher the conductivity. The energy of formation was calculated in order to determine the thermodynamic stability of these $Li_5La_3Zr_{2-x}Ta_xO_{12}$ structures. The results show that all three structures have negative energy of formation, which implies that the structures are thermodynamically stable. The $Li_5La_3ZrTaO_{12}$ (P1) structure has the lowest energy of formation which makes it more thermodynamically stable than the $Li_5La_3Zr_{0.5}Ta_{1.5}O_{12}$ (C2/c) and $Li_5La_3Zr_{0.25}Ta_{1.75}O_{12}$ (P1) structures. Long-term cycling stability requires a sufficient electrolyte volume. Having less electrolyte increases ohmic and charge transfer resistances. Moreover, lithium dendrites will form when the electrolyte volume is low. The calculated volume of the $Li_5La_3Zr_{2-x}Ta_xO_{12}$ structures is half the volume of pure t-LLZO as it has half the amount of atoms, this is because the doped structure has a 4-formula unit cell while the pure structure has a 8-formula unit cell, however, both structures have sufficient volume for application in a solid-state batteries.

4.4.5. Elastic Properties of Ta-doped LLZO

Elasticity is a property of materials that determines their mechanical strength. Elastic constants are the constants that describe the mechanical response of a material. The elastic constants measure the proportionality between strain and stress in a crystal, provided that the strain is not so large as to violate Hook's law. Elastic modulus denotes the material's resistance to elastic deformation. The elastic modulus parameters are calculated to give a clear analysis of the materials stability when under pressure and stress.

The bulk modulus is one of the most important parameters that characterize the physical property of a material system because it also measures the degree of stiffness or the energy required to produce a given volume deformation, while shear modulus describes the resistance to shape change caused by shearing force; young's modulus reflects the resistance of materials against tensions. As an indicator of hardness and strength, the bulk modulus is the inverse of compressibility. It exhibits the bonding characteristics in the material. In his work, Pugh introduced the bulk-shear modulus ratio of polycrystalline phases (B/G), according to which the shear modulus represents the resistance to plastic deformation, while the bulk modulus represents the resistance to fracture.

In general, a high B/G value indicates ductility, while a low value indicates brittleness. The critical value for separating brittleness from ductility is 1.75. Basically, elastic constants of a material describe its response to externally applied strain or the stress required to maintain a given deformation and provide useful information of the strength of the material, as characterized by Bulk modulus (B), shear modulus (C), Young's modulus (E), Pugh ratio (B/G) and Poisson's ratio (v). This section provide a detailed analysis of the elastic constants and elastic modulus obtained through first-principles DFT elastic properties calculations. The shear modulus (G), Bulk modulus (B), Young's modulus (E), Pugh's ratio (B/G), and Poisson's ratio (v) are discussed for a better understanding of the mechanical stability of the CE generated Ta-doped structure against deformation.

4.4.4.1. Elastic Constants

Table 4.6: Calculated elastic constants (C_{11}, C_{12}, C_{13}, C_{22}, C_{23}, C_{33}, C_{44}, C_{55} and C_{66}) of Ta doped LLZO structures.

	$Li_5La_3ZrTaO_{12}$ (P1)	$Li_5La_3Zr_{0.5}Ta_{1.5}O_{12}$ (C2/c)	$Li_5La_3Zr_{0.25}Ta_{1.75}O_{12}$ (P1)
C_{11}	154.48	167.77	184.17
C_{12}	85.41	86.21	88.88
C_{13}	78.53	79.80	78.62
C_{22}	154.40	164.36	181.51
C_{23}	78.52	77.97	78.28
C_{33}	195.16	205.74	222.52
C_{44}	59.42	64.76	73.02
C_{55}	50.31	67.47	77.72
C_{66}	30.64	44.11	69.43

(i) $Li_5La_3ZrTaO_{12}$

The elastic constants are calculated to determine the mechanical stability of the crystal structure using the generalised gradient approximation. Table 4.6 show the calculated elastic constants results of $Li_5La_3ZrTaO_{12}$ oxide solid electrolyte structures. From table 4.6, it is observed that the elastic constants C_{ij} for $Li_5La_3ZrTaO_{12}$ structure are positive which is content with the stability conditions. Moreover, the calculated elastic constants satisfy the necessary Born stability conditions listed below which indicate a good mechanical stability of the $Li_5La_3ZrTaO_{12}$ material.

The necessary and sufficient Born criteria for triclinic P1 structure are given by: [68]

$$2C^2_{16} < C_{66} (C_{11} - C_{12})$$

$$C_{22}C_{33} - C^2_{23} > 0; C_{33}C_{55} - C^2_{35} > 0; C_{44}C_{66} - C^2_{46} > 0$$

$$C_{11} + C_{22} + C_{33} + 2(C_{12} + C_{13} + C_{23}) > 0 \quad (4\text{-}2)$$

(ii) $Li_5La_3Zr_{0.5}Ta_{1.5}O_{12}$

Table 4.6 show the calculated elastic constants results of $Li_5La_3Zr_{0.5}Ta_{1.5}O_{12}$ structure. The elastic constants for $Li_5La_3Zr_{0.5}Ta_{1.5}O_{12}$ structure are higher than the elastic constants result of $Li_5La_3ZrTaO_{12}$ structure. Moreover, the elastic constants values for $Li_5La_3Zr_{0.5}Ta_{1.5}O_{12}$ structures are similar to the results of the pure t-LLZO structure, and are all positive which is content with the stability conditions. The $Li_5La_3Zr_{0.5}Ta_{1.5}O_{12}$ structure is mechanically stable since the elastic constants are all positive and satisfy the necessary criterions given below.

The necessary and sufficient Born criteria for monoclinic C2/c structure are given by: [68]

$C_{11} > 0; C_{11}C_{22} > C^2_{12}$

$C_{11}C_{22}C_{33} + 2C_{12}C_{13}C_{23} - C_{11}C^2_{23} - C_{22}C^2_{13} - C_{33}C^2_{12} > 0$ (4-3)

$C_{44} > 0; C_{55} > 0; C_{66} > 0$

(iii) $Li_5La_3Zr_{0.25}Ta_{1.75}O_{12}$

The elastic constants C_{ij} for $Li_5La_3Zr_{0.25}Ta_{1.75}O_{12}$ are shown in table 4.6 above. From the results, it is observed that the elastic constants for $Li_5La_3Zr_{0.25}Ta_{1.75}O_{12}$ are much higher compared to the elastic constant of $Li_5La_3ZrTaO_{12}$, and $Li_5La_3Zr_{0.5}Ta_{1.5}O_{12}$ structures. Moreover, the elastic constants of $Li_5La_3Zr_{0.25}Ta_{1.75}O_{12}$ are higher than that of pure t-LLZO which implies a good improvement of the elastic constants, also all the values are positive indicating a good mechanical stability of the material. It is clear that when the concentration of tantalum increases so does the elastic constants. The mechanical stability of the structure was further analysed based on the Born stability criterions, and the $Li_5La_3Zr_{0.25}Ta_{1.75}O_{12}$ elastic constant results are content with the necessary Born criterions.

The necessary and sufficient Born criteria for triclinic P1 structure are given by: [68]

$2C^2_{16} < C_{66} (C_{11} - C_{12})$

$C_{22}C_{33} - C^2_{23} > 0; C_{33}C_{55} - C^2_{35} > 0; C_{44}C_{66} - C^2_{46} > 0$

$C_{11} + C_{22} + C_{33} + 2(C_{12} + C_{13} + C_{23}) > 0$ (4-4)

4.4.4.2 Elastic Moduli

Table 4.7: Calculated Bulk (B), Shear (G), Young modulus (E), and Pugh ratio (B/G) modulus of Ta doped LLZO using GGA approximation.

	$Li_5La_3ZrTaO_{12}$ (P1)	$Li_5La_3Zr_{0.5}Ta_{1.5}O_{12}$ (C2/c)	$Li_5La_3Zr_{0.25}Ta_{1.75}O_{12}$ (P-1)
Bulk modulus B (GPa)	109.47	113.29	119.72
Shear modulus G (GPa)	43.65	53.65	65.79
Young modulus E (GPa)	115.57	139.06	166.80
Pugh ratio B/G	2.51	2.12	1.82
Poisson's ratio v	0.32	0.30	0.27

(i) $Li_5La_3ZrTaO_{12}$

Table 4.7 shows the elastic moduli results of $Li_5La_3ZrTaO_{12}$ structure. The bulk modulus is calculated to measure the ability of the material to withstand change in volume when under compression on all sides. A material that is easy to compress has a high compressibility but a low bulk modulus. From the table 4.7, $Li_5La_3ZrTaO_{12}$ has a bulk modulus of 109.47 GPa. The large bulk modulus of the $Li_5La_3ZrTaO_{12}$ structure implies that the material has the ability to return to its original volume after the applied pressure is removed, in other words, the material is incompressible. To check the structure's resistance against deformation, shear modulus was calculated. From the results in table 4.7, it is clear that $Li_5La_3ZrTaO_{12}$ structure has a large shear modulus which implies that it is stiff enough to resist deformation. The material has a sufficient shear modulus to prevent Li dendrite nucleation in a battery according to the stability criterion of Monroe and Newman [71]. The Young's modulus was calculated to measure the compressive stiffness of the material. From table 4.7, $Li_5La_3ZrTaO_{12}$ structure has a young's modulus of 115.57 GPa. This implies that the material does not break when bent or stretched. In order to determine the ductility or brittleness of the $Li_5La_3ZrTaO_{12}$ structure, the Pugh's ratio (B/G) was calculated. A material is considered ductile if B/G is greater than 1.75, and brittle if less than 1.75. From the table 4.7, the $Li_5La_3ZrTaO_{12}$ structure has a Pugh's ratio of 2.51 which is greater than 1.75, this implies that the material is ductile. The $Li_5La_3ZrTaO_{12}$ structure has a Poisson's ratio of 0.32 which implies that the material is ductile and ionic, this is in good agreement with the above analysis of Pugh's ratio results.

(ii) $Li_5La_3Zr_{0.5}Ta_{1.5}O_{12}$

The calculated bulk modulus (B), shear modulus (G), Young's modulus (E), Poisson's ratio (v), and Pugh ratio (k=B/G) results of $Li_5La_3Zr_{0.5}Ta_{1.5}O_{12}$ structure are shown in table 4.7. From the results it is observed that the calculated bulk modulus of $Li_5La_3Zr_{0.5}Ta_{1.5}O_{12}$ is higher than that of $Li_5La_3ZrTaO_{12}$ structure, which indicate that the material has the ability to withstand compression. Also, the $Li_5La_3Zr_{0.5}Ta_{1.5}O_{12}$ structure has sufficient shear and young's modulus suggesting great stiffness stability of the material against deformation. The calculated results of Pugh and Poisson ratios shown in table 4.7 indicate that $Li_5La_3Zr_{0.5}Ta_{1.5}O_{12}$ is ductile and ionic.

(iii) $Li_5La_3Zr_{0.25}Ta_{1.75}O_{12}$

The $Li_5La_3Zr_{0.25}Ta_{1.75}O_{12}$ structure has similar elastic moduli results as $Li_5La_3ZrTaO_{12}$ and $Li_5La_3Zr_{0.5}Ta_{1.5}O_{12}$ structures, shown in table 4.7, which implies that the structures have similar mechanical properties in terms of hardness, fracture toughness, stiffness and many more. The $Li_5La_3Zr_{0.25}Ta_{1.75}O_{12}$ structure has the highest bulk, shear and young's moduli which makes it the stiffest and tough compare to the other structures. From the results, it is observed that the elastic moduli increase with an increase in the Ta concentration which is expected since tantalum is highly resistant to corrosion. Moreover, comparing the calculated elastic moduli of $Li_5La_3Zr_{0.25}Ta_{1.75}O_{12}$ structure and that of the pure tetragonal LLZO, there is an improvement in the elastic results of the doped $Li_5La_3Zr_{0.25}Ta_{1.75}O_{12}$ structure which is due to the tantalum since it has greater mechanical stability against deformation.

4.4.6. Electronic Properties of Ta-doped LLZO

A material's electronic characteristics are a set of parameters and representations that explain how electrons interact with it. Based on the electron energy bandgap, the band structure helps visualize whether the materials are conductors, insulators, or semiconductors. Instead of discrete energy levels, atoms in free form have a band of energy available. Electrons must be present in the conduction band for the conduction process to work. The valence and conduction bands are separated by a huge gap in insulators, metals have a valence band that overlaps the conduction band, and semiconductors have a narrow gap between the two bands that is bridged by thermal or other excitation. When atoms are grouped together to create a solid, quantum mechanical forces enable these discrete energy levels to be disrupted, and the electrons in the collection of individual atoms inhabit the solid's valence band. Every atom's empty states expand into a band of levels that is normally empty, known as the conduction band. Similarly, electrons in atoms can go from one energy level to another in the same band or in a different band, often crossing a forbidden energy gap in the process. The electronic behaviour of Ta-doped $Li_5La_3Zr_{2-x}Ta_xO_{12}$ was studied using first-principle DFT calculations under the generalized gradient approximation (GGA). This section contains a detailed discussion of the calculated band structure plots.

4.5.1 Band Structure

The band structures were calculated in order to evaluate the electronic behaviour of the solid-state electrolyte materials. In the curves of the band structures, the energy function is plotted in the first brillouin zone versus the energy (eV). From this diagram, some important information on the crystal-electronic nature of being metal or non-metal, the energy gap gage can be obtained if it exists, the type of energy gap being direct or indirect, the effective mass, the velocity and mobility of the carrier and so on. Figure 4.4 (a-c) show the band structure plots of the $Li_5La_3Zr_{2-x}Ta_xO_{12}$ structures. The band structures were calculated at equilibrium pressure using GGA approximation. The bands below zero line are the valence bands and above the zero line are the conduction bands. The distance between the states at the valence band maxima

(VBM) and the conduction band minima (CBM) is determined by the electronic band gap."According to the below plotted band structures, all the $Li_5La_3Zr_{2-x}Ta_xO_{12}$ structures have direct band gaps of ~4.6 eV located along the G-symmetry point of the brillouin zone. Compared to the band gap of the pure t-LLZO (discussed in chapter 3), there is an improvement in the band gaps of the Ta-dope structures. This is because the bond distance between Li-Li in doped Ta-LLZO is smaller than in pure t-LLZO which mean that the electrons are more tightly bound to the atom, and hence require more energy to remove, leading to an increased band gap. The large band gap imply that the structures are magnetic separators with a wide electrochemical window. Thus, the $Li_5La_3Zr_{2-x}Ta_xO_{12}$ structures are electronically stable, facilitating its use in next-generation batteries.

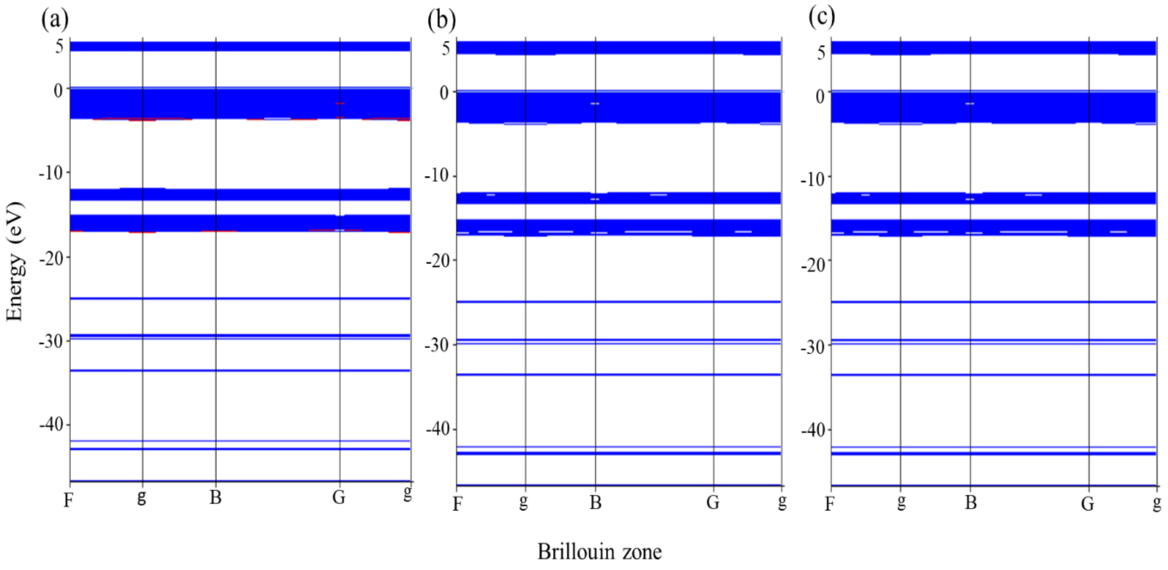

Figure 4.4: The band structures of Ta-doped $Li_5La_3Zr_{2-x}Ta_xO_{12}$ (x = 1, 1.5 and 1.75) solid state electrolytes (a) $Li_5La_3ZrTaO_{12}$ (P1) (b) $Li_5La_3Zr_{0.5}Ta_{1.5}O_{12}$ (C2/c) (c) $Li_5La_3Zr_{0.25}Ta_{1.75}O_{12}$ (P1)

CHAPTER 5: Research summary and conclusion.

Summary and Conclusion

For a viable solid-state electrolyte, high ionic conductivity is not the only requirement: it must also be stiff enough to suppress Li dendrite formation during cycling and have a wide electrochemical window to prevent electronic leakage. Consequently, the structural, elastic, and electronic properties of solid electrolytes are a highly important feature in the design of all-solid-state batteries, despite sometimes being overlooked. The thesis provides an overall perspective on the properties of the oxide garnet solid-state electrolyte. Accurate results were obtained through the use of first-principle techniques. The cut-off energy and the k-mesh point sufficient to converge the oxide garnet were determined to be 500 eV and 5x5x5, respectively. Afterward, the structure was optimized to relax the atoms in the t-LLZO crystal, allowing the cell volume and the lattice parameters to reach their ground state energies. It was found that the calculated lattice parameters and volume are in good agreement with experimental results. The heat of formation of t-LLZO is negative, indicating good thermodynamic stability.

Further calculations of the elastic constants and elastic modulus were performed for analysis of the mechanical stability of t-LLZO. It was found that all the necessary and sufficient elastic constants are positive which is consistent with the stability conditions. Additionally, the elastic constants satisfy the Born criteria which imply good mechanical stability of tetragonal LLZO. The elastic modulus gives an insight into the mechanical behaviour of t-LLZO. The calculated bulk modulus suggests that t-LLZO has the ability to return to its original volume after the applied pressure is removed, in other words, t-LLZO is incompressible. To check the structure's resistance against deformation, the shear modulus was calculated, and it was found that t-LLZO has a sufficient shear modulus to prevent Li dendrite nucleation in a battery according to the stability criterion. Moreover, the calculated elastic moduli are in good agreement with other computational and experimental results, suggesting a good mechanical behaviour of t-LLZO.

The electronic behaviour of t-LLZO was analysed in a form of band structure and density of state. The band structure showed a large band gap along the gamma-symmetry point, which confirms the magnetic separator behaviour of t-LLZO. Moreover, the large band gap indicates a wide electrochemical window which is an intrinsic property for electrolyte materials, facilitating its use in next-generation batteries. The density of state (DOS) confirms the band structure predictions, since there was a large band gap formed at the p orbital of the Li atom, and the energy of the band gap is similar to that predicted by the band structure.

Cluster expansion calculations were performed on the t-LLZO to generate new possible phases of Ta-doped LLZO. The binary ground state diagram obtained from CE calculations were discussed in detail for a better understanding of how the structures are generated. The ground-state search generated 28 new multi-component thermodynamically stable structures with negative enthalpy of formation. Only 5 structures were considered the most stable by CE on the ground-state line. All the generated new structures have a cross validation score (CVS) of less than 5meV, indicating accuracy in CE calculations. Moreover, this implies good functionality of the generated phases in a practical setting. Predicting the phase stability of Ta-doped LLZO is crucial for materials design and development. The MC temperature profile obtained from MC simulations, showed that at concentrations $Zr_{0.5}Ta_{0.5}$, $Zr_{0.25}Ta_{0.75}$ and $Zr_{0.125}Ta_{0.875}$ the systems mix very well at temperatures 800K, 1000K and 800K, respectively. The systems showed no phase separation with a very small energy difference of 0.9eV/atom, 0.61eV/atom, and 0.45eV/atom, respectively, indicating a homogeneous mixture of the systems.

Further DFT calculations were performed on the most generated stable $Li_5La_3Zr_{2-x}Ta_xO_{12}$ (x = 1, 1.5 and 1.75) structures to determine the structural, mechanical, and electronic properties of the structures for their use as active solid-state electrolyte. The lattice parameters of the $Li_5La_3Zr_{2-x}Ta_xO_{12}$ (x = 1, 1.5 and 1.75) structures decrease with an increase in tantalum concentration. This indicate an improvement in the generated crystal structures stability and the conductivity of the structures, since the bond length between Li-Li in Ta-doped systems is smaller than in pure t-LLZO. As a result, the $Li_5La_3Zr_{2-x}Ta_xO_{12}$ (x = 1.75) structure with the highest tantalum concentration was found to have the lowest energy of formation compared to the pure t-LLZO structure and the other Ta-doped structures, which makes it the most stable thermodynamically. Additionally, the $Li_5La_3Zr_{2-x}Ta_xO_{12}$ (x = 1.75) structure showed a great improvement in terms of elastic constants and elastic modulus, suggesting greater resistance to deformation when under stress or pressure. Consequently, the electronic stability of the structure also improved with band gap increase, indicating a magnetic separator behaviour with a wide electrochemical window.

Overall, the present study concludes that pure and Ta-doped LLZO structures exhibit good structural, mechanical, and electronic stability, moreover the findings provide a better understanding of the phase stability of the generated Ta-doped LLZO structures, paving the way for further research and development of these promising materials.

Recommendations and future work

The study of oxide garnet solid-state electrolytes remains relevant in the energy storage industries. The current findings on both pure and Ta-doped LLZO structures have shown similar trends with regard to elastic and electronic behaviour. However, various properties such as the crystal structure Li-ion transport mechanism at high temperature are necessary to assist in the interpretations of the current results, especially for the stable CE generated Ta-doped structures. The results also showed improvement in the property calculations of Ta-doped structures. Thus, there is a need for further calculations in this regard: introduce another dopant (W) and evaluate the phase properties to gain more understanding of the doping process and Li-ion transport mechanism.

In the study, ab-initio molecular dynamics simulation will be performed on the tetragonal LLZO and Ta/W-doped LLZO to gain insight into their phase transformation as a function of temperature under micro-canonical NVT and canonical NVE ensemble. The simulation will also facilitate attaining the rate of lithium-ion diffusion and the mobility of the lanthanum, zirconium, tantalum, and oxygen ions in the system at high temperatures. The study will contribute to the deep understanding of the ionic conductivity and stability of oxide garnet for further development of the advanced solid-state electrolytes in the energy storage field.

The future work will focus on the following aspects:

Determine the effect of temperature on the t-LLZO and Ta/W-LLZO structures under the NVT and NVE ensemble, investigate the lithium diffusion mechanism of the structures, and perform amorphization and recrystallization of t-LLZO and $Li_5La_3Zr_{2-x}M_xO_{12}$ (M= Ta and W) nanoparticles.

References

[1] X. Fan, B. Liu, J. Liu, J. Ding, X. Han, Y. Deng, X. Lv, Y. Xie, B. Chen, W. Hu and C. Zhong, (2020) "Battery Technologies for Grid-Level Large-Scale Electrical Energy Storage," *Springer Ser.Chem. Phys.,* **26**, 92-103.

[2] J.B Goodenough, (2018) “How we made the Li-ion rechargeable battery,” *Nature elctronics,* **1**, 204.

[3] S. Ramakumar, C. Deviannapoorani, L. Dhiyva, L.S. Shankar, and R. Murugan, (2017) “lithium garnets: synthesis, structure, Li^+ dynamics and applications,” *Prog. Mater. Sci.,* **180**, 37-42.

[4] H. Duan, H. Zheng, Y. Zhou, B. Xu and H. Liu, (2018) “Stability of garnet-type Li ion conductors: An overview,” *solid state ionics,* **318**, 45-53.

[5] B. Wu, S. Wang, W. J. Evans IV , D. Z. Deng, J. Yang and J. Xiao, (2016) “Interfacial behaviours between lithium ion conductors and electrode materials in various battery systems,” *J. Mater. Chem. A.,* **4**, 15266-15280.

[6] N. Nitta, F. Wu, J.T. Lee, and G. Yushin, (2015) “Li-ion battery materials: present and future,” *Mater. Today,* **18**, 252-264.

[7] A. Kato, M. Yamamoto,F. Utsuno, H. Higuchi, and M. Takahashi, (2021) “Lithium-ion-conductive sulfide polymer electrolyte with disulfide bond-linked PS4 tetrahedra for all-solid-state batteries,” *Communications Materials,* **2**, 112.

[8] M. V. Reddy, C. M. Julie, A. Mauger, and K. Zaghib, (2020) “Sulfide and Oxide Inorganic Solid-state Electrolytes for All-Solid-State Li Batteries: A Review,” *Nanomaterials,* **10**, 1606.

[9] W. Zhao, J. Yi, P. He, and H. Zhou, (2019) “Solid-State Electrolytes for Lithium-Ion Batteries: Fundamentals, Challenges and Perspectives,” *Springer,* **2**, 574–605.

[10] Y. M. Lee, J. E. Seo, N.-S. Choi, and J.-K. Park, (2005) “Influence of tris(pentafluorophenyl) borane as an anion receptor on ionic conductivity of $LiClO_4$-based electrolyte for lithium batteries.,” *Electrochim. Acta,* **50**, 2843–2848.

[11] M. L. Lehmann, G. Yang, D. Gilmer, K. S. Han, E. C. Self, R. E. Ruther, et al., (2019) “Tailored crosslinking of Poly(ethylene oxide) enables mechanical robustness and improved sodium-ion conductivity.,” *Energy Storage Mater.,* **21**, 85–96.

[12] J. Awaka, A. Takashima, K. Kataoka, N. Kijima, Y. Idemoto, and J. Akimoto, (2011) "Crystal structure of fast lithium-ion-conducting cubic LLZO," *Chem. Lett.,* **40**, 60-62.

[13] R. Murugan, V. Thangadurai and W. Weppner, (2007) "Fast lithium ion conduction in garnet-type $Li_7La_3Zr_2O_{12}$.," *Angew. Chem., Int. Ed. Engl.,* **46**, 7778-7781.

[14] J. Awaka, N. Kijima, H. Hayakawa, and J. Akimoto, (2009) "Synthesis and structure analysis of tetragonal $Li_7La_3Zr_2O_{12}$ with the garnet-related type structure," *J. Solid State Chem,* **182**, 2046–2052.

[15] H. Buschmann, J. Dolle, S. Berendts, A. Kuhn, P. Bottke, M. Wilkening, P. Heitjans, A. Senyshyn, H. Ehrenberg, A. Lotnyk, V. Duppel, L. Kienle, and J. Janek, (2011) "Structure and dynamics of the fast lithium ion conductor $Li_7La_3Zr_2O_{12}$" *Phys. Chem. Chem. Phys,* **13**, 19378–19392.

[16] K. B. Dermenci, E. Cekic, and S. Turan, (2016) "Al stabilized $Li_7La_3Zr_2O_{12}$ solid electrolytes for all-solid state Li-ion batteries," *Int. J. Hydrog. Energy,* **41**, 9860-9867.

[17] M. R. Bonilla, F. A. Garcia Daze, J. Carrasco, and E. Akhmatskaya, (2019) "Exploring Li-ion conductivity in cubic, tetragonal and mixed-phase Al-substituted $Li_7La_3Zr_2O_{12}$ using atomistic simulations and effective medium theory," *Acta Materialia,* **175**, 426-435.

[18] J. E. Ni, E. D. Case, J. S. Sakamoto, E. Rangasamy, and J. B. Wolfenstine, (2012) "Room temperature elastic moduli and Vickers hardness of hot-pressed LLZO cubic garnet," *J. Mater. Sci,* **47**, 7978-7985.

[19] E. Yi, W. Wang, J. Kieffer, and R. M. Laine, (2016) "Flame made nanoparticles permit processing of dense, flexible, Li^+ conducting ceramic electrolyte thin films of cubic-$Li_7La_3Zr_2O_{12}$ (c-LLZO)," *J. Mater. Chem. A,* **4**, 12947-12954.

[20] A. Orera, G. Larraz, J. A. Rodriguez-Velamazan, J. Campo, and M. L. Sanjuan, (2016) "Influence of Li^+ and H^+ distribution on the crystal structure of $Li_{(7-x)}H_{(x)}La_3Zr_2O_{12}$ ($0 \leq x \leq 5$) garnets," *Inorg. Chem.,* **55**, 1324-1332.

[21] C. A. Geiger, E. Alekseev, B. Lazic, M. Fisch, T. Armbruster, R. Langner, M. Fechtelkord, N. Kim, T. Pettke, and W. Weppner, (2011) "Crystal chemistry and

stability of "$Li_7La_3Zr_2O_{12}$" garnet: a fast lithium-ion conductor," *Inorg. Chem.,* **50**, 1089-1097.

[22] W. Xia, B. Xu, H. Duan, Y. Guo, H. Kang, H. Li, and H. Liu, (2016) "Ionic conductivity and air stability of Al-doped $Li_7La_3Zr_2O_{12}$ sintered in alumina and Pt crucibles," *ACS Appl. Mater. Interfaces,* **8**, 5335-5342.

[23] Y. Zhang, F. Chen, and J. Li, (2018) "Regulation Mechanism of Bottleneck Size on Li^+, Migration Activation Energy in Garnet-Type $Li_7La_3Zr_2O_{12}$.," *Electrochim Acta.,* **261**, 137-142.

[24] J. Wolfenstine, E. Rangasamy, J. L. Allen, and J. Sakamoto, (2012) "High conductivity of dense tetragonal $Li_7La_3Zr_2O_{12}$," *J. Power Sources,* **208**, 193-196.

[25] A. Düvel, and A. Kuhn, (2012) "Mechanosynthesis of Solid Electrolytes: Preparation, Characterization, and Li Ion Transport Properties of Garnet-Type Al-Doped $Li_7La_3Zr_2O_{12}$ Crystallizing with Cubic Symmetry," *J. Phys. Chem. C.,* **116**, 15192-15202.

[26] J. F. Wu, W. K. Pang, V. K. Peterson, L. Wei, and X. Guo, (2017) "Garnet-Type Fast Li-Ion Conductors with High Ionic Conductivities for All-Solid-State Batteries," *ACS Appl Mater Interface,* **9**, 12461-68.

[27] L. J. Miara, W. D. Richards, Y. E. Wang, and G. Ceder, (2015) "First-principles studies on cation dopants and Electrolyte|Cathode interphases for lithium garnets," *Chem. Mater.,* **27**, 4040-4047.

[28] C. Bernuy-Lopez, W. Manalastas, J. M. L. del Amo, A. Aguadero, F. Aguesse, and J. A. Kilner, (2014) "Atmosphere controlled processing of Ga-substituted garnets for high Li-ion conductivity ceramics," *Chem. Mater.,* **26**, 3610-3617.

[29] D. O. Shin, K. Oh, K. M. Kim, K. -Y. Park, B. Lee, Y. -G. Lee, and K. Kang, (2015) "Synergistic multi-doping effects on the $Li_7La_3Zr_2O_{12}$ solid electrolyte for fast lithium ion conduction," *Sci. Rep.,* **5**, 18053.

[30] R. H. Brugge, J. A. Kilner, and A. Aguadero, (2019) "Germanium as a donor dopant in garnet electrolytes," *solid state ionics,* **337**,154-160.

[31] Y. Cao, Y.-Q. Li, and X.-X. Guo, (2013) "Densification and lithium ion conductivity of garnet-type $Li_{7-x}La_3Zr_{2-x}Ta_xO_{12}$ (x = 0.25) solid electrolytes," *Chin. Phys.,* **22**, 078201.

[32] M. Huang, W. Xu, Y. Shen, Y.-H. Lin, and C.-W. Nan, (2014) "X-ray absorption near-edge spectroscopy study on Ge-doped $Li_7La_3Zr_2O_{12}$: enhanced ionic conductivity and defect chemistry," *Electrochim. Acta,* **115**, 581-586.

[33] N. Janani, C. Deviannapoorani, L. Dhivya, and R. Murugan, (2014) "Influence of sintering additives on densification and Li + conductivity of Al doped $Li_7La_3Zr_2O_{12}$ lithium garnet," *RSC Adv.,* **4**, 51228-51238.

[34] L. Dhivya, K. Karthik, S. Ramakumar, and R. Murugan, (2015) "Facile synthesis of high lithium ion conductive cubic phase lithium garnets for electrochemical energy storage devices," *RSC Adv.,* **5**, 96042-96051.

[35] H. El Shinawi and J. Janek, (2013) "Stabilization of cubic lithium-stuffed garnets of the type "$Li_7La_3Zr_2O_{12}$" by addition of gallium," *J. Power Sources,* **225**, 13-19.

[36] J. Wolfenstine, J. Ratchford, E. Rangasamy, J. Sakamoto, and J.L. Allen, (2012) "Synthesis and high Li-ion conductivity of Ga-stabilized cubic $Li_7La_3Zr_2O_{12}$," *Mater. Chem. Phys.,* **134**, 571-575.

[37] K. Liu and C.-A. Wang, (2014) "Garnet-type $Li_{6.4}La_3Zr_{1.4}Ta_{0.6}O_{12}$ thin sheet: fabrication and application in lithium-hydrogen peroxide semi-fuel cell," *Electrochem. Commun.,* **48**, 147-150.

[38] H. El-Shinawi, E. J. Cussen, and S. A. Corr, (2019) "Enhancement of the lithium ion conductivity of Ta-doped $Li_7La_3Zr_2O_{12}$ by incorporation of calcium," *Dalton Trans.,* **46**, 9415-9419.

[39] Y. Jin and P. McGinn, (2011) "Al-doped $Li_7La_3Zr_2O_{12}$ synthesized by a polymerized complex method," *J. Power Sources,* **196**, 8683-8687.

[40] A. A. Raskovalov, E. A. Il'ina, and B. D. Antonov, (2013) "Structure and transport properties of Li7La3Zr2-0.75xAlxO12 superionic solid electrolytes," *J. Power Sources,* **238**, 48-52.

[41] G. Kresse, and J. Furthermuller, (1996) *Phys Rev.*, **154**, 11169-11188.

[42] D. R. Hartree, (1928) “The Wave Mechanics of an Atom with a Non-Coulomb Central Field. Part I. Theory and Methods,” *Mathematical Proceedings of the Cambridge Philosophical Society,* **24**, 89-110.

[43] J. P. Perdew and Y. Wang, (1992) *Phys. Rev. B,* **45**, 13244.

[44] P. Hohenberg and W. Kohn, (1964) “Inhomogeneous Electron Gas,” *Phys. Rev.,* **136**, B864 - B871.

[45] M. Chakraverty, H. M. Kittur, and P. A. Kumar, (2013) “First Principle Simulations of Various Magnetic Tunnel Junctions for Applications in Magnetoresistive Random Access Memories,” *IEEE Trans. Nanotechnol.,* **12**, 971.

[46] K. Horn and M. Scheffler, (2000) “In Electronic Structure,” *Handbook of Surface Science,* **2**.

[47] D. J. W. Geldart and M. Rasolt, (1976) “Exchange and correlation energy of an inhomogeneous electron gas at metallic densities,” *Phys. Rev. B.,* **13**, 1477.

[48] G. P. Robert, and Y. Weitao, (1994) “Density-Functional Theory of Atoms and Molecules,” *Oxford: Oxford University Press*.

[49] P. A. M. Dirac, (1930) “Note on Exchange Phenomena in the Thomas-Fermi Atom,” *Proc. Cambridge Phil. Roy. Soc.,* **26**, 385.

[50] D. M. Ceperley and B. J. Alder, (1980) “Ground state of the electron gas by a stochastic method,” *Phys. Rev.,* **45**, 556-559.

[51] A. D. Becke, (1998) “Density-functional exchange-energy approximation with correct asymptotic behavior,” *Phys. Rev.,* **38**, 3098–3100.

[52] D. Lerch, O. Wieckhorst, G. L. W. Hart, R. W. Forcade, and S. Muller, (2009) "Modelling simulation of material science engineering," **17**, 055003.

[53] J. M. Sanchez, F. Ducastelle, and D. Gratias, (1984) "Physica A: Statistical and Thoeretical Physics," **128**, 334.

[54] A. Mark, D. de Fontaine, M. van Schilfgaarde, M. Sluiter, and M. Methfessel, (1992) *Phys. Rev. B.*, **46**, 5055.

[55] C. Colinet, A. Pasturel, D. Nguyen Manh, D. G. Pettifor, and P. Miodownik, *Phys. Rev. B.,* **56**, 552.

[56] M. Asta, R. McCormack, and D. de Fontaine, (1993) *Phys. Rev. B.,* **48**, 748.

[57] D. Lerch, O. Wiekhorst, G. L. W. Hart, R. W. Forcade, and S. Muller, (2009) "UNCLE: a code for constructing cluster expansions for arbitrary lattices with minimal user-input," *Modelling Simul. Mater. Sci. Eng.,* **17**, 330.

[58] G. L. W. Hart, V. Blum, M. J. Walorski, and A. Zunger, (2005) "Evolutionary approach for determining first-principles hamiltonians," *Nature Mat.,* **4**, 391.

[59] D. Reith and R. Podloucky, (2009) "First-principles model study of the phase stabilities of dilute Fe-Cu alloys: Role of vibrational free energy," *Phys. Rev. B,* **80**, 054108.

[60] H. F. Monkhorst and J. D. Park, (1976) "Special points for Brillouin-Zone integrations.," *Phys. Rev. B,* **13**, 5188-5192.

[61] N. Hiroshi, H. Toshiaki and Y. Teijiro, (1981) "Molecules in an electric field. Model for molecular geomeetry," *J. Am. Chem. Soc.,* **103**, 7426-7432.

[62] N. L. Lethole, (2015) "Computer Modelling Studies of MPO_4, $LiMPO_4$ and $NaMPO_4$ (M: Fe, Co, Mn) Polymorphs,"

[63] S. Kamran, K. Chen and L. Chen, (2009) "Ab-initio examination of ductility features of fcc metals.," *Phys. Rev. B,* **79**, 379-393.

[64] R. Hill, (1952) "The elastic behavior of a crystalline aggregate.," *Proc. Phys. Soc. A,* **65**, 349-364.

[65] R. B. Kaner, J. J. Gilman and S. H. Tolbert, (2005) "Designing superhard materials.," *Mat. Scie.,* **308**, 1268-1269.

[66] "Wikimedia Commons. (2015). Band Gap Comparison [Online]. Available: https://upload.wikimedia.org/wikipedia/commons/thumb/0/0b/Band_gap_comparison.svg/2000px-Band_gap_comparison.svg.png".

[67] S. Yu, R. D. Schmidt, R. Garcia-Mendez, E. Herbert, N. J. Dudney, J. B. Wolfenstine, J. Sakamoto, and D. J. Siegel, (2016) "Elastic Properties of the Solid Electrolyte Li7La3Zr2O12 (LLZO)," *Chem. Mater.,* **28**, 197.

[68] F. Mouhat and F. -X Coudert, (2014) "Necessary and sufficient elastic stability conditions in various crystal systems," *Phys. Rev. B ,* **90**, 224104.

[69] S. F. Pugh, (1954) "XCII. Relations between the elastic moduli and the plastic properties of polycrystalline pure metals," *Philos. Mag. Ser.,* **45**, 823-843.

[70] S. C. Abrahams and J. L. Bernstein, (1971) "Rutile: normal probability plot analysis and accurate measurement of crystal structure," *J. Chem. Phys,* **55**, 3206 - 3211.

[71] C. Monroe and J. Newman, (2005) "The Impact of Elastic Deformation on Deposition Kinetics at Lithium/Polymer Interfaces," *J. Electrochem. Soc.,* **2**, 152.

Appendix

Papers presented at conferences

1. R.I. Maphoto, M.C. Masedi, P. E. Ngoepe, and R.S. Ledwaba, "Computational Modelling Study on the Stability of Ta Doped Tetragonal $Li_7La_3Zr_2O_{12}$ Oxide Garnet for Solid-State Li batteries" *South African Institute of Physics (SAIP)*, Virtual by SAIP, July 2021.

2. R.I. Maphoto, K.T. Malatji, M.C. Masedi, P. E. Ngoepe, and R.S. Ledwaba, “Phase Stability of Ta-Doped Tetragonal $Li_7La_3Zr_2O_{12}$ Solid-State Electrolyte for Li-ion batteries Using Cluster Expansion and Monte-Carlo Techniques” *Faculty of Science and Agriculture Research Day (FSA)*, Bolivia Lodge, Polokwane, October 2021.
3. R.I. Maphoto, M.C. Masedi, P. E. Ngoepe, and R.S. Ledwaba, “First-Principles Study on Structural, Mechanical and Electronic Properties of $Li_7La_3Zr_2O_{12}$ Solid Electrolyte” *Conference of the South African Advanced Materials Initiative (CoSAAMI)*, Virtual by CSIR, MINTEK and NECSA, October 2021.
4. R.I. Maphoto, K.T. Malatji, M.C. Masedi, P. E. Ngoepe, and R.S. Ledwaba, “First-Principle Cluster Expansion Study of Ta-Substituted Tetragonal $Li_7La_3Zr_2O_{12}$ (t-LLZO) Oxide-Garnet Solid-State Electrolyte.” *Centre of High performance and Computing (CHPC)*, Virtual by CHPC, December 2021.
5.

Published papers

1. R. Maphoto, M. Masedi, P. Ngoepe and R. Ledwaba, (2021) First-principles study on structural, mechanical and electronic properties of $Li_7La_3Zr_2O_{12}$ solid electrolyte. *Suid-Afrikaans Tydskrif vir Natuurwetenskap en Tegnologie/South African Journal of Science and Technology*, *40*, 12-15.
2.